



저작자표시-비영리-변경금지 2.0 대한민국

이용자는 아래의 조건을 따르는 경우에 한하여 자유롭게

- 이 저작물을 복제, 배포, 전송, 전시, 공연 및 방송할 수 있습니다.

다음과 같은 조건을 따라야 합니다:



저작자표시. 귀하는 원저작자를 표시하여야 합니다.



비영리. 귀하는 이 저작물을 영리 목적으로 이용할 수 없습니다.



변경금지. 귀하는 이 저작물을 개작, 변형 또는 가공할 수 없습니다.

- 귀하는, 이 저작물의 재이용이나 배포의 경우, 이 저작물에 적용된 이용허락조건을 명확하게 나타내어야 합니다.
- 저작권자로부터 별도의 허가를 받으면 이러한 조건들은 적용되지 않습니다.

저작권법에 따른 이용자의 권리는 위의 내용에 의하여 영향을 받지 않습니다.

이것은 [이용허락규약\(Legal Code\)](#)을 이해하기 쉽게 요약한 것입니다.

[Disclaimer](#)

공학박사 학위논문

**Charged Aerosol Generation via
Spark Discharge and Its
Applications**

스파크 방전을 이용한 하전 에어로졸 발생 및

그 응용

2012 년 8 월

서울대학교 대학원

기계항공공학부

한 규 희

This page is intended to be blank

스파크방전을 이용한 하전
에어로졸 발생 및 그 응용

**Charged Aerosol Generation via Spark Discharge
and Its Applications**

지도 교수 최 만 수

이 논문을 공학박사 학위논문으로 제출함
2012 년 4 월

서울대학교 대학원
기계항공공학부
한 규 희

한규희의 공학박사 학위논문을 인준함
2012 년 7 월

위 원 장 _____ 이 정 훈 _____ (인)

부위원장 _____ 최 만 수 _____ (인)

위 원 _____ 전 누 리 _____ (인)

위 원 _____ 서 갑 양 _____ (인)

위 원 _____ 김 태 성 _____ (인)

This page is intended to be blank

Charged Aerosol Generation via Spark Discharge and Its Applications

Kyuhee Han

School of Mechanical and Aerospace Engineering

The Graduate School

Seoul National University

Abstract

Nanoparticles have been widely studied in nanotechnology due to their unique characteristics. Establishment of reliable and robust nanoparticle patterning methodology is a prerequisite for practical use of the nanoparticles, which could be a promising alternative to conventional photolithography. High resolution and parallel patterning of charged aerosols via Ion-Assisted Aerosol Lithography (IAAL) was previously reported and has been utilized for unique three-dimensional patterning of nanoparticles as well as conventional two-dimensional patterning on conducting substrates. Stable preparation of charged aerosols and their patterning regardless of the kind of substrates could expand the application of the IAAL in nanotechnology. This study is aimed to develop an unconventional type spark discharge generator as a facile charged aerosol provider for the IAAL and extend the limitation of the IAAL for charged particle patterning even on a non-conducting substrate. The new type spark discharge generator was applied to fabricate nanoparticle

embedded organic light emitting diode (OLED) for enhancement of light emission efficiency.

Much smaller unagglomerated charged metal aerosols with a narrower size distribution at higher concentration were obtained via a pin-to-plate type spark discharge generator in comparison to the conventional rod-to-rod type generators. The sizes and charge distributions of particles were measured and compared for In-Sn alloy, silver and copper. Spark parameters and flow pattern for each configuration were investigated to explain the observed phenomena. Much faster transport of as-generated particles in the pin-to-plate type electrode configuration played a critical role in producing smaller and unagglomerated charged aerosols in comparison to the rod-to-rod type generator. It was also found that charge distribution of generated particles via the rod-to-rod type generator was changed with respect to spark frequency in contrast with our spark discharge generator because the characteristic of electro-deposition of charged particles to the electrode was changed depending on the spark frequency.

A method of patterning of charged aerosols on a non-conducting substrate using a focusing mask was developed. The temporary path to neutralize the charge of particles was devised to eliminate the charges from incoming charged particles by forming the conductive liquid film on the substrate. This was done by using a surfactant and droplets via electrospraying liquid. Nano and micro scaled patterns were demonstrated with PolyStyrene Latex (PSL) particles via this method. Conducting micro wires with silver nanoinks were easily produced with a higher resolution in compared to normal inkjet technology. Sub-micro scaled patterns were also realized with charged metal particles generated by spark discharge generator.

Unagglomerated gold aerosols via the pin-to-plate type spark discharge generator were utilized to increase the external quantum efficiency (EQE) for an OLED. The gold aerosols were easily embedded in the middle of organic materials of the OLED at a desired position without damage to the organic material with our newly developed spark generator. The optimum size of the

particles at a known optimum position was engineered to maximize the EQE of the OLED and the corresponding enhancement of EQE was about 44 %. Maximum of EQE could be attributed to optimized equilibrium between the balance of charge carriers and the reduction of the area for recombination site of holes and electrons in the OLED.

Keywords: Spark discharge; Charged aerosols; Ion-assisted aerosol lithography; Organic light emitting diode;

Student Number: 2008-30202

Contents

Abstract	i
Contents	iv
List of Tables	vii
Nomenclature	viii
List of Figures	xi
Chapter 1. Introduction	1
1.1. Background of Research	2
1.2. Objectives for Research	8
1.3. Scope of Research	9
1.4. References	11
Chapter 2. Charged Aerosol Generation via Spark Discharge	15
2.1. Introduction.....	16
2.2. Experimental Concept.....	19
2.2.1. Spark discharge	19
2.2.2. Pin-to-Plate type spark discharge generator	21
2.2.3. Electric circuit for spark discharge.....	23
2.2.4. Measurement of sizes and charge distribution of particles	24
2.3. Results and discussion	28
2.3.1. Less agglomerated aerosol via Spark Discharge	28
2.3.2. Electrical response during spark discharge	33
2.3.3. Charge distribution of generated particles.....	34
2.3.4. Spark parameter analysis.....	36
2.3.5. Flow pattern in spark discharge generators	40

2.3.6. Change in charge distribution of particles.....	45
2.4. Conclusion	55
2.5. References.....	56
Chapter 3. Focused Patterning of Charged Nanoparticles on a Non-Conducting Substrate.....	59
3.1. Introduction.....	60
3.2. Experimental Concepts	64
3.2.1. Focused Patterning of charged particles on a non- conducting substrate.....	64
3.2.2. Prerequisites for focused patterning of charged particles on a non-conducting substrate.....	66
3.3. Experimental setup.....	68
3.3.1. Surface active agent (Surfactant)	69
3.3.2. Ion-induced Nanoparticle Focusing Mask	70
3.3.3. Preparation of liquid droplet and charged particles.....	72
3.4. Results and discussion	75
3.4.1. Formation of conducting liquid film	75
3.4.2. Focused patterning on a non-conducting substrate	77
3.5. Conclusion	83
3.6. References.....	84
Chapter 4. Enhancement of Luminescence of OLED using Gold Nanoparticles	87
4.1. Introduction.....	88
4.2. Background and Experimental Procedure.....	90
4.2.1. Fluorescence of organic material	90
4.2.2. OLED fabrication with gold nanoparticles	92
4.3. Results and Discussions.....	98

4.3.1. The sizes of gold nanoparticles with respect to spark parameters.	98
4.3.2. Characteristics of OLED with respect to the sizes of gold nanoparticles.....	103
4.4. Conclusion	112
4.5. References.....	113
Chapter 5. Concluding Remarks	117
Acknowledgement	121
Abstract(in Korean)	122

List of Tables

Table 2.1. Properties of gases at Standard Conditions: 294.3K, 1 atm (Schmid et al. 2002).....	26
Table 3.1. Electrospray condition with respect to liquids.	73
Table 3.2. Droplet size calculated from scaling law.....	74

Nomenclature

C_c	Cunningham correction factor	
C_{ext}	external capacitance	[F]
d_0	Debye length of plasma	[m]
d_A	Debye length of plasma at anode	[m]
d_C	Debye length of plasma at cathode	[m]
d_g	geometric mean diameter	[nm]
d_p	particle diameter	[nm]
D_d	droplet diameter	[cm]
e	charge of an electron	$[1.602 \times 10^{-19} \text{ C}]$
E_s	electric field between positive electrode and plasma	[V/m]
E_0	maximum electric field	[V/m]
G	constant in droplet diameter calculation	
K	electrical conductivity of liquid	[S/m]
L	column length in DMA	[m]
n	number of elementary charge	

\mathbf{n}	normal vector perpendicular to the substrate	
\mathbf{p}_{eff}	effective electric dipole moment	[Cm]
Q	liquid flow rate	[cc/sec]
Q_{sh}	sheath flow rate in DMA	[liter/min]
R_c	charging resistance	[ohm]
R_{inner}	inner radius of column in DMA	[m]
R_{outer}	outer radius of column in DMA	[m]
V	voltage applied to DMA	[V]
$V_{electrode}$	potential applied to electrode	[V]
V_{HV}	applied setting potential of HV source	[V]
v_p	velocity of particle	[V]
V_{HV}	applied setting potential from HV	[V]
Z_p	electrical mobility of particle	[m ² /V·s]

Greek Symbols

γ	balance of charge carriers in OLED	
ε_0	permittivity of free space	$[8.854 \times 10^{-12} \text{ F/m}]$
ε_l	dielectric constant of liquid	
η_{oc}	out-coupling efficiency of OLED	
η_s	production efficiency of singlet for fluorophores	
μ	viscosity of the gas	$[\text{N}\cdot\text{s}/\text{m}^2]$
μ_p	electrical mobility of particle	$[\text{m}^2/\text{V}\cdot\text{s}]$
σ_g	geometric standard deviation	
λ	mean free path	$[\mu\text{m}]$
τ_s	spark relaxation time	$[\text{sec}]$
φ	quantum efficiency of fluorescence	

List of Figures

Figure 1.1 Mechanisms of vapor and particle production (nucleation), growth, charging and transport in atmospheric pressure electrical discharge. (Adapted from Borra 2006).....	4
Figure 2.1. A conventional spark discharge generator (Adopted from Schwyn et al. 1988.).....	17
Figure 2.2. Characteristic of Voltage and current during discharge (Adopted from http://www.plasma-universe.com).....	20
Figure 2.3. Two different configurations of spark discharge generator. (A) pin-to-plate type electrode configuration. (B) rod-to-rod type electrode configuration. (Adopted from Han et al 2012).....	21
Figure 2.4. Schematic of electric circuit for spark discharge system.....	23
Figure 2.5. Experimental schematic for particle measurement system.	27
Figure 2.6. In-Sn alloy nanoparticles generated by spark discharge generator with a gap distance of 2.5 mm, argon gas flow rate of 3.5 lpm and applied positive potential of 5 kV. (A) A TEM image of particles for pin-to-plate type SDG. (B) A TEM image of particles for rod-to-rod type SDG (C) PAED based size distributions (D) Mobility diameter based size distributions. (Adopted from Han et al 2012)	29
Figure 2.7. Silver and copper nanoparticles generated by spark discharge with a gap distance of 2.5 mm, argon gas flow rate of 3.5 lpm and applied positive potential of 5 kV. (A) A TEM image of silver particles for pin-	

to-plate type SDG. (B) A TEM image of silver particles for rod-to-rod type SDG. (C) PAED based size distributions of silver particles. (Adopted from Han et al 2012)	31
Figure 2.8. Silver and copper nanoparticles generated by spark discharge with a gap distance of 2.5 mm, argon gas flow rate of 3.5 lpm and applied positive potential of 5 kV. (A) A TEM image of copper particles for pin-to-plate type SDG. (B) A TEM image of copper particles for rod-to-rod type SDG. (C) PAED based size distributions of copper particles. (Adopted from Han et al 2012)	32
Figure 2.9. Electrical responses during spark discharge. (A) Voltage oscillation with respect to time defining spark frequency (B) Voltage and current oscillation during spark discharge. (Adopted from Han et al 2012)	33
Figure 2.10. Current versus electrical mobility for positively and negatively charged particles of In-Sn alloy for each configuration with a gap distance of 2.5 mm, argon gas flow rate of 3.5 lpm and applied positive potential of 5 kV. (Adopted from Han et al 2012).....	35
Figure 2.11. Spark parameters and electric field strength for each configuration (A) Spark energy and spark frequency versus applied positive potentials for different configurations (B) the calculated electrical field strength between the gap of electrodes and equi-potential lines (insets) between the electrodes along the dashed lines for different configurations with the applied positive potential of 2.7 kV. (Adopted from Han et al 2012)	37

Figure 2.12. The calculated electrical field strength between the electrodes with respect to the radius of curvature of pin electrode for pin-to-plate electrode with the same condition as Fig. 2.11B..... 39

Figure 2.13 Flow fields near particle generation and coagulation zone for each configuration. Insets show colour plots of velocities up to 3 m/s emphasizing high velocities (red colour) between electrode gap of PP-SDG and low velocities (blue colour) between electrode gap of RR-SDG (A) Velocity and its contour in cross-sectional view (inset) near particle generation zone for pin-to-plate configuration. (B) Velocity and its contour in cross-sectional view (inset) near particle generation and coagulation zone for rod-to-rod configuration. (Adopted from Han et al 2012) 41

Figure 2.14. Pin-to-Rod type electrode configuration and charged particle generation during spark discharge with silver. (A) Pin-to-rod type electrode configuration. (B) Current versus electrical mobility for positively and negatively charged particles of silver for three different types of configuration with a gap distance of 2.5 mm, argon gas flow rate of 3.5 lpm and applied positive potential of 5 kV..... 42

Figure 2.15. Post-discharge neutralization in RR-SDG (A) The schematic of post-discharge neutralization by ions in slow transport zone in RR-SDG (B) The experimentally determined bipolar charge distribution of aerosol particles in argon (Adoped from Wiedensohler, A. and Fissan, H., 1991). 44

Figure 2.16. Change in charge distribution of particles via the RR-SDG with

InSn alloy with respect to spark frequency (A) Charge distribution of particles with respect to spark frequency with a gap distance of 2.5 mm, argon gas flow rate of 3.5 lpm and applied positive potential of 5 kV (B) Change in the ratio of number concentration of negatively charged particles and that of positively charged particles with respect to spark frequency.	46
Figure 2.17. Characteristic of voltage and current during spark discharge and change in potential of the positive electrode. (A) Profiles of voltage and current with millisecond scale in SDGs. (B) Increase of potential of positive electrode at spark relaxation time.	48
Figure 2.18. Schematic of electro-deposition of charged particles in a plasma on the electrodes during spark discharge.	50
Figure 2.19. Characteristic of electro-deposition of charged particles. (A) Electro-deposition of the charged particles with respect to the capacitance in the spark circuit. (B) Electro-deposition of the charged particles with respect to the mobility of the charged particles. (Assume $E_0 = 1E6$ V/m).....	52
Figure 2.20. Charge distribution of particles via RR-SDG with InSn alloy with respect to electrical polarity with a gap distance of 2.5 mm, argon gas flow rate of 3.5 lpm and applied positive potential of 5 kV.	53
Figure 2.21. Charge distribution of particles via PP-SDG with InSn alloy with respect to electrical polarity with a gap distance of 2.5 mm, argon gas flow rate of 3.5 lpm and applied positive potential of 5 kV.	54
Figure 3.1. Ion-Assisted Aerosol Lithography. (A) Schematic of the principle	

of IAAL (B) SEM image of patterns via IAAL (Adopted from Kim et al. 2006).	61
Figure 3.2. Limitation of IAAL method with respect to dielectric thickness on a conducting substrate. (A-C) the Focusing effect of IAAL increases as dielectric thickness on a conducting substrate increases. (D) Distortion of electric field line with 8 μm thick dielectric destroys ion induced focusing lens and nanoparticles are no longer deposited on the substrate. (Adopted from You et al.)	63
Figure 3.3. Schematic of focused patterning of charged particles on a non-conducting substrate. (Adopted from You et al. 2010)	64
Figure 3.4. Three critical factors for patterning on a non-conducting substrate via the IAAL. (A) Surfactant modifying hydrophilicity of the surface of the substrate. (B) Nanoparticle focusing mask substituting PR pre-patterns and forming electrostatic focusing lens by ion accumulation for the IAAL. (C) Charged particles and droplets supplied via electrospray during deposition.	67
Figure 3.5. Schematic of experimental setup for the patterning	68
Figure 3.6. Surfactant. (Nonylphenoxyethoxylates)	69
Figure 3.7. Fabrication procedure for silicon nitride mask used in the experiment.	71
Figure 3.8. Schematic of charged particle deposition via electrospray of conducting liquid on a substrate.	72
Figure 3.9. Schematic of experimental setup for checking connectivity.	76
Figure 3.10. Current measurement through the temporary conducting film. (A)	

Schematic of experimental setup. (B) Current measured with respect to surface treatment of the substrate.....	76
Figure 3.11. Patterns of PSL particles on the thick glass. (A) Optical image of 0.7 mm thick glass substrate. (B) SEM image of the silicon nitride mask having line type openings (C) 420 nm line patterns consisting of 30 nm-sized PSL particles. (Adopted from You et al. 2010).....	77
Figure 3.12. Patterns of PSL particles on the flexible PET film. (A) Optical image of 0.1 mm flexible PET film. (B) Photography of the epoxy mask (C) 10 μm line patterns and 12 x 12 μm^2 consisting of 100 nm-sized PSL particles. (Adopted from You et al. 2010).....	78
Figure 3.13. Patterning of a micro conducting wire with silver ink on the Kapton film. (A) Schematic of experimental setup. (B) SEM image of the 8 μm wide conducting wire. (C) Voltage and current relation for the conducting wire and inset shows the epoxy mask used for patterning. (Adopted from work with J. Lee).....	80
Figure 3.14. Patterning of gold nanoparticles generated via spark discharge generator on the PET film. (A) Schematic of experimental setup. (B) SEM image of the 270 nm line patterns. (C) 350 x 350 nm^2 square patterns.....	82
Figure 4.1. The Jablonski diagram displaying the energy states of a molecule. (Adopted from Lichtman and Conchello, 2005).....	90
Figure 4.2. The Organic Light Emitting Diode fabricated in the experiment. (A) The schematic of the OLED configuration. (B) Molecular structure of Alq3 used as both emitting layer and electron transfer layer. (C)	

Molecular structure of NPB.	92
Figure 4.3. Energy band diagram for the organic bylayer of OLED fabricated in the experiment. (A) Energy band of the OLED without electrical potential. (B) Energy band bending of the OLED with electrical potential and the resultant recombination.	93
Figure. 4.4. Schematic of experimental equipment for gold nanoparticle deposition in the middle of the NPB film of the OLED.....	95
Figure 4.5. Control of the sizes of nanoparticles in spark discharge. (A) Size control by changing capacitance in the circuit. (B) Size control by changing the flow rate of the carrier gas.	97
Figure 4.6. Gold nanoparticles generated by spark discharge generators with a gap distance of 1 mm, N ₂ gas flow rate of 2 lpm and applied positive potential of 5kV. (A) TEM images of gold nanoparticles for PPSDG and RRS DG. (B) Mobility diameter based size distribution for both configurations.....	99
Figure 4.7. Mobility diameter based size distribution with respect to the capacitance in the electrical circuit.	100
Figure 4.8. Gold nanoparticles generated adjusting the capacitances of the external capacitor. (A,D) TEM and SEM images of gold nanoparticles via the SDG with nitrogen flow rate of 2 lpm, resistance of 20 Mohm and capacitance of 2 nF. (B,E) TEM and SEM images of gold nanoparticles via the SDG with resistance of 10 Mohm and capacitance of 4 nF. (C,F) TEM and SEM images of gold nanoparticles via the SDG with resistance of 5 Mohm and capacitance of 8 nF.	101

Figure 4.9. Gold nanoparticles generated adjusting the flow rate of carrier gas.
 (A) A TEM image (B) A SEM image (C) Mobility based size distribution of gold nanoparticles via the SDG with resistance of 20 Mohm and capacitance of 2 nF depending on nitrogen flow rate..... 102

Figure 4.10. Characteristics of the OLED devices with respect to capacitance in the electric circuit (A) Characteristics of current density versus voltage driving the device. (B) External quantum efficiency of the devices. ... 104

Figure 4.12. Characteristics of the OLED devices with respect to N₂ flow rate.
 (A) Characteristics of current density versus voltage driving the devices. (B) External quantum efficiency of the devices. 105

Figure 4.12. Photoluminescence spectra of the OLEDs with the particles deposited at the distance of 20 nm from the emitting layer and the OLED without the particles. Inset shows the schematic of photoluminescence measurement using excitation source wavelength of 430 nm. 107

Figure 4.13. Extinction and absorption in the NPB layer with gold nanoparticles. (A) Extinction spectrum of gold nanoparticles deposited at the distance of 20 nm from the emitting layer in middle of the NPB layer. (B) Calculated absorption of NPB layer with gold nanoparticles with respect to size of a gold particle. 110

Figure 4.14. Electric fields in the OLED with fully charged gold nanoparticles and external potential of 7 V. (A) Electric fields in the OLED with 6 nm-sized gold nanoparticles at the distance of 20 nm from the emitting layer in middle of the NPB layer. (B) Electric fields in the OLED with 10 nm-sized gold nanoparticles at the same position as the case of 6 nm-sized

particles. (C) Electric fields at cathode and anode with respect to particle sizes comparing to the case without the particles..... 111

This page is intended to be blank

Chapter 1.

Introduction

1.1. Background of Research

Nanoparticle patterning has been widely studied as one of the promising alternatives to photolithography. Many researches on the patterning have been dealt with nanoparticles dispersed in aqueous or organic solvents with stabilization by surfactants (Liao et al. 2012; Son et al. 2011; Sung et al. 2012). Those nanoparticles are synthesized in various chemical ways in liquid but have inherent impurities such as stabilizers or surfactants accompanying by their production process. Various liquid-based patterning technologies, such as micro transfer molding, micro-molding, micro contact printing and nanoimprinting, represented by “Soft Lithography” have shown possibility and various applications. (Duan et al. 2010; Park et al. 2008; Wang et al. 2009) On the other side, gas phase particle syntheses also have been developed with advantages in terms of pure particle generation without impurities (Biskos et al. 2008; Borra 2006; Kruis et al. 1998). Gas-phase synthesized particles have been exploited for nanoparticle patterning by controlling the behavior of nanoparticles with electrical field (Krinke et al. 2002; Sung et al. 2012; Wang et al. 2009). Parallel and high resolution nanoparticle focused patterning with ion-induced electric field has been studied with aerosol technology (Kim et al. 2006; Lee et al. 2010; You et al. 2010). Ion-assisted aerosol lithography (IAAL) is the focused patterning of charged particles using electrostatic lens formed by ion accumulation on the dielectric surface like a photoresist, which can guide and control the particle into wanted position.

Nanoparticle patterning via IAAL has significant prerequisites, which are composed of a number of charged particles, conductive substrates neutralizing incoming charged particles, ions for building electrostatic lens, and pre-patterned dielectric surface for ion accumulation and guidance of nanoparticles. Therefore, preparation of charged particles is one of the significant factors of IAAL. Charged particle generation has two distinct process composed of particle generation and particle charging (Borra 2006; 2008). A lot of particle generation methods have been reported but particle charging is not as numerous as particle generation. Diffusion charging and field charging are accomplished through high electric field or residence in plentiful ion clouds for suitable time, respectively (Borra 2008; Hinds 1999). Electro-hydrodynamic atomization easily prepares charged particles from particles dispersed in conducting solvents (Cloupeau and Prunetfoch 1994; La Mora and Fernandez 1994; Lenggoro et al. 2002). Conducting solvent, material stabilization in liquids, and relatively resultant large agglomerate of particles could limit the advantages of electrospray method. In addition, electrospray is not easy to be applied to the non-conducting liquids in which many liquid processed nanoparticles are dispersed under stabilization by surfactants.

Electrical discharges have been exploited to generate nanoparticles and their aggregates, and to deposit films on substrates, as shown in Fig. 1.1. Spark discharge (Byeon et al 2008; Helsper et al. 1993; Roth et al. 2004; Schwyn et al. 1988; Tabrizi et al. 2009) could be a good candidate method

for generating charged nanoparticles for aerosol patterning, which has simultaneous particle generation and charging in the plasma formed during spark discharge. In addition, particles have narrower size distribution and their sizes could be controlled by parameters defining spark discharge (Tabrizi et al. 2009). Nanoparticles are easily generated via evaporation of electrode material by heat and ion sputtering during spark discharge. However, the as-generated particles via a conventional rod-to-rod type spark discharge often tend to get agglomerates (Bau et al. 2010). The generation of unagglomerated charged particle at high concentration via spark discharge is highly desirable in order to broaden its applications in nanotechnology and to establish spark discharge as a robust method in gas phase particle synthesis.

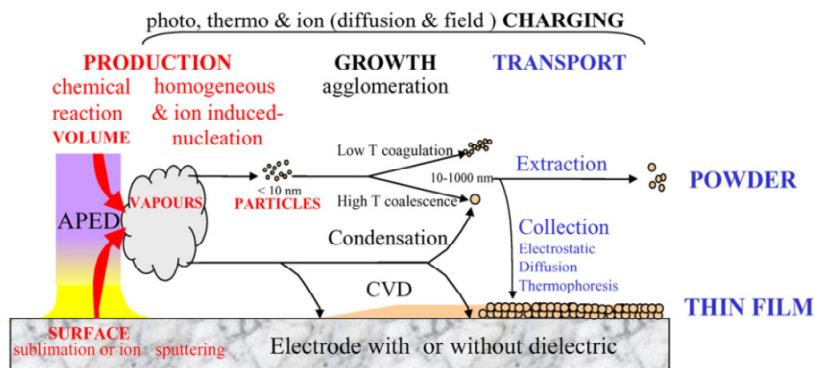


Figure 1.1 Mechanisms of vapor and particle production (nucleation), growth, charging and transport in atmospheric pressure electrical discharge. (Adapted from Borra 2006)

Studies of charged particle generation via spark discharge have been rare even though spark discharge have been known to generate charged particles (Borra 2006; Tabrizi et al. 2009). Therefore, characteristics of charged particles generation via SDG are deserved to be investigated further.

Up to date, IAAL has been well utilized for multi-dimensional patterning on conducting substrates. The patterning limited to the conducting substrates could confine the potential of the methods. Patterning of those charged nanoparticles on the non-conducting substrates is essential for enlargement of application of the IAAL. Precise positioning and arrangement of nanoparticles on non-conducting substrates such as thick glass or flexible polymer film have been needed for the production of nano-electronics and cost-effective nanodevices. Charged particle patterning on non-conducting substrates via controlled electric field is a challenge because neutralization of incoming charged nanoparticles is essential for the successive patterning on the non-conducting substrates. Therefore, the patterning method applying IAAL to non-conducting substrates is needed to be developed.

Metal nanoparticles have been widely used to increase efficient of OLED with the principle of localized surface plasmon resonance (LSPR) (Fujiki et al. 2010; Tanaka et al. 2011), which have been extensively engineered to enhance efficiency of light emission or absorption in optic devices (Okamoto et al. 2004; Schuller et al. 2010) as well as for bio-sensing / imaging (Hutter and Fendler 2004) and Raman spectroscopy (Campion and Kambhampati

1998). Another interesting phenomenon for metal nanoparticles is charge trapping or charge blocking behavior in the OLED. (Li et al. 2008) Wet-processed gold nanoparticles have typically been utilized to enhance the emission efficiency of OLED. (Fujiki et al. 2010) Positioning the nanoparticles in the middle of the OLED is very important to optimize the LSPR effect or the charge trapping effect considering quenching effect of metal particles. However, wet-processed metal nanoparticles are difficult to be deposited on organic materials without contamination or damage to them. Aerosol based metal nanoparticles could be applicable to any position in the OLED devices without any stabilizer or surfactant. Especially, the spark discharge generator was used positioning them at desired positions in middle of the organic materials with a facile way and engineering the optimum position for maximizing the efficiency of OLED (Sung, H et al 2012). The influence of the sizes of metal nanoparticles on the emission efficiency of OLED at a known optimum position is needed to study further in order to find out the optimum size at the optimum position because spark discharge can easily control their sizes with spark parameters

In this study, we developed an unconventional type spark discharge generator for producing less agglomerated nanoparticles. Nanoparticles via the generator could be exploited as precise building block for the IAAL. Also, we obtained focused patterning of spark generated particle on a non-conducting substrate by forming temporary conducting liquid film, which follows principal concepts of the IAAL and enables high resolution

patterning on the non-conducting substrate. Lastly, nanoparticles via the generator were applied to increase the efficiency of the OLED and their effects on the emission enhancement of the OLED were studied.

1.2. Objectives for Research

In this research, we pursue developing an efficient generation method of charged nanoparticles used as building blocks and eliminating the restriction of the IAAL for non-conducting substrates. To realize the goals, we develop a facile spark generator for less agglomerated and charged nanoparticles. Next, we conceived a conducting path for charge neutralization on the surface of the non-conducting substrate. Also, we found another application utilizing those nanoparticles.

First, preparation of unagglomerated charged particles is one of essential factors for aerosol based nanoparticle patterning. Particle generation via spark discharge satisfies the need in a facile way because the generation and charging of those nanoparticles are accomplished via spark discharge, simultaneously.

Second, charged particle patterning on a non-conducting substrate have been still challenging unless charge neutralization and prevention of resultant repulsion between particles with same polarity are prepared. We proposed the temporary path to eliminate the charges from incoming charged particles by forming the conductive liquid film on the substrate.

Finally, those unagglomerated metal particles would be exploited to enhance the emission efficiency of electroluminescence devices utilizing charge carrier trapping or blocking behavior by the particles.

1.3. Scope of Research

Unagglomerated charged particles were obtained through an unconventional electrode type spark discharge generator, and focused patterning of charged nanoparticles was realized on non-conducting substrates utilizing a temporary conducting liquid film. Those charged nanoparticles were utilized for optic devices using their unique electrical effects including localized surface plasmon resonance effect and charge trapping effect.

Generation of unagglomerated charged particles is a critical factor for precise aerosol based nanoparticle patterning. Particle production by spark discharge has been known as a facile and reliable method generating nanometer sized particles. However, a conventional rod-to-rod type spark discharge generator presents agglomerate of particles unless high flow rate of a carrier gas is supplied. We develop an unconventional type spark discharge generator for producing less agglomerated nanoparticles and compare it with a conventional type spark discharge generator in terms of sizes and charge distribution of the particles in chapter 2. Also, changes in charge distribution of particles via the rod-to-rod type generator were investigated.

For focused patterning of particles on a non-conducting substrate, we proposed the temporary path to eliminate the charges from incoming charged particles by forming the conductive liquid film on the substrate in chapter 3. Formation of conductive liquid film on the substrate is based on hydrophilic

characteristic of the surface. We used a surfactant to change the hydrophobic into hydrophilic surface. The droplets of conducting liquids via electrospray were supplied and the droplets formed thin film on the hydrophilic surface. Nano and micro scaled patterns were obtained with PolyStyrene Latex (PSL) particles via this method, and conducting micro wires with silver nanoinks were patterned with several micro-sized resolutions. Sub-micro scaled gold nanoparticle patterns also were realized with charged particles via spark discharge generator.

In chapter 4, we proposed application of those unagglomerated particles to the OLED to enhance its efficiency utilizing charge trapping behavior even though LSPR effect of the particles was not dominant. Organic LED was fabricated with NPB as a hole transfer layer and Alq3 for both light emitting layer and electron transfer layer. Gold nanoparticles via our spark discharge generator were easy to be placed at a known optimum position in the middle of organic layer in contrast with other nanoparticle fabrication method without damage of organic material. LSPR effect of gold nanoparticles near the emitting layer was considered and charge trapping effect of the metal particles was also studied qualitatively. The optical and electrical effects of those nanoparticles on external quantum efficiency were evaluated.

Finally, we summarize and conclude the results and discussion of this study in chapter 5.

1.4. References

- Bau, S., Witschger, O., Gensdarmes, F., Thomas, D. and Borra, J. (2010). Electrical properties of airborne nanoparticles produced by a commercial spark-discharge generator. *Journal of Nanoparticle Research*, 1-7.
- Biskos, G., Vons, V., Yurteri, C. U. and Schmidt-Ott, A. (2008). Generation and sizing of particles for aerosol-based nanotechnology. *KONA Powder Particle J*, 26, 13-35.
- Borra, J. (2006). Nucleation and aerosol processing in atmospheric pressure electrical discharges: powders production, coatings and filtration. *Journal of Physics D: Applied Physics*, 39, R19.
- Borra, J. (2008). Charging of aerosol and nucleation in atmospheric pressure electrical discharges. *Plasma Physics and Controlled Fusion*, 50, 124036.
- Byeon, J., Park, J., Yoon, K. and Hwang, J. (2008). Site-Selective Catalytic Surface Activation via Aerosol Nanoparticles for Use in Metal Micropatterning. *Langmuir*, 24, 5949-5954.
- Campion, A., Kambhampati, P. (1998). Surface-enhanced Raman scattering. *Chemical Society Review*, 27, 241.
- Cloupeau, M. and Prunetfoch, B. (1994). Electrohydrodynamic spraying functioning modes – a critical review. *Journal of Aerosol Science*, 25, 1021-1036.
- Duan, X., Zhao, Y., Berenschot, E., Tas, N. R., Reinhoudt, D. N. and Huskens, J. (2010). Large Area Nanoscale Patterning of Functional Materials by Nanomolding in Capillaries. *Advanced Functional Materials*, 20, 2519-2526.

- Fujiki, A., Uemura, T., Zettsu, N., Akai-Kasaya, M., Saito, A. and Kuwahara, Y. (2010). Enhanced fluorescence by surface plasmon coupling of Au nanoparticles in an organic electroluminescence diode. *Applied Physics Letters*, 96, 043307-043307-043303.
- Hinds, W. C. (1999). *Aerosol technology: properties, behavior, and measurement of airborne particles* (2nd).
- Hutter, E., Fendler, J. H. (2004). Exploitation of Localized Surface Plasmon Resonance. *Advanced materials*, 16, 1685.
- Kim, H., Kim, J., Yang, H., Suh, J., Kim, T., Han, B., Kim, S., Kim, D. S., Pikhitsa, P. V. and Choi, M. (2006). Parallel patterning of nanoparticles via electrodynamic focusing of charged aerosols. *Nature Nanotechnology*, 1, 117-121.
- Krinke, T. J., Deppert, K., Magnusson, M. H., Schmidt, F. and Fissan, H. (2002). Microscopic aspects of the deposition of nanoparticles from the gas phase. *Journal of Aerosol Science*, 33, 1341-1359.
- Kruis, F. E., Fissan, H. and Peled, A. (1998). Synthesis of nanoparticles in the gas phase for electronic, optical and magnetic applications - A review. *Journal of Aerosol Science*, 29, 511-535.
- La Mora, D. and Fernandez, J. (1994). The current emitted by highly conducting Taylor cones. *Journal of Fluid Mechanics*, 260, 155-184.
- Lee, H., You, S., Pikhitsa, P. V., Kim, J., Kwon, S., Woo, C. G. and Choi, M. (2010). Three-Dimensional Assembly of Nanoparticles from Charged Aerosols. *Nano Letters*, 11, 119-124.
- Lenggoro, I. W., Xia, B., Okuyama, K. and de la Mora, J. F. (2002). Sizing of

- colloidal nanoparticles by electrospray and differential mobility analyzer methods. *Langmuir*, 18, 4584-4591.
- Li, W., Pan, S. and Rothberg, L. J. (2008). Emissive Efficiency Enhancement of Alq₃ and Prospects for Plasmon-enhanced Organic Electroluminescence, Society of Photo-Optical Instrumentation Engineers, 703224.703221-703224.703227.
- Liao, J., Li, X., Wang, Y., Zhang, C., Sun, J., Duan, C., Chen, Q. and Peng, L. (2012). Patterned Close-Packed Nanoparticle Arrays with Controllable Dimensions and Precise Locations. *Small*.
- Okamoto, K., Niki, I., Shvarts, A., Narukawa, Y., Mukai, T. and Scherer, A. (2004). Surface-plasmon-enhanced light emitters based on InGaN quantum wells. *Nature materials*, 3, 601-605.
- Park, I., Ko, S. H., Pan, H., Grigoropoulos, C. P., Pisano, A. P., Fréchet, J. M. J., Lee, E. S. and Jeong, J. H. (2008). Nanoscale patterning and electronics on flexible substrate by direct nanoimprinting of metallic nanoparticles. *Advanced Materials*, 20, 489-496.
- Schuller, J. A., Barnard, E. S., Cai, W., Jun, Y. C., White, J. S. and Brongersma, M. L. (2010). Plasmonics for extreme light concentration and manipulation. *Nature materials*, 9, 193-204.
- Son, Y., Yeo, J., Moon, H., Lim, T. W., Hong, S., Nam, K. H., Yoo, S., Grigoropoulos, C. P., Yang, D. Y. and Ko, S. H. (2011). Nanoscale Electronics: Digital Fabrication by Direct Femtosecond Laser Processing of Metal Nanoparticles. *Advanced Materials*.
- Sung, H., Lee, J., Han, K., Kim, C. and Choi, M. (2012). , Quantun efficiency

enhancement in a gold nanoparticle-embedded organic light emitting device engineering the particle position. In preparation.

Sung, S. H., Yoon, H., Lim, J. and Char, K. (2012). Reusable Stamps for Printing Sub-100 nm Patterns of Functional Nanoparticles. *Small*.

Tanaka, T., Totoki, Y., Fujiki, A., Zettsu, N., Miyake, Y., Akai-Kasaya, M., Saito, A., Ogawa, T. and Kuwahara, Y. (2011). Enhanced Red-Light Emission by Local Plasmon Coupling of Au Nanorods in an Organic Light-Emitting Diode. *Applied Physics Express*, 4, 2105.

Wang, Y. H., Mirkin, C. A. and Park, S. J. (2009). Nanofabrication beyond electronics. *ACS nano*, 3, 1049-1056.

You, S., Han, K., Kim, H., Lee, H., Woo, C. G., Jeong, C., Nam, W. and Choi, M. (2010). Nanoparticle patterning: High-Resolution, Parallel Patterning of Nanoparticles via an Ion-Induced Focusing Mask. *Small*, 6, 2146-2152.

Chapter 2.

Charged Aerosol Generation via Spark Discharge

2.1. Introduction

Charged nanoparticles have been widely used for bottom-up nanoparticle patterning with electric forces, and the generation of those particles is one of the important factors in the patterning. Spark discharge at atmosphere (Schwyn et al. 1988) is a facile and reliable method for generating nanometer-sized particles among various gas phase synthesis methods (Biskos et al. 2008; Kruis et al. 1998). The method has advantages generating charged aerosols with a simple set-up, which can be exploited to construct nanostructures via controlled electric field (Krinke et al. 2002; Kim et al. 2006; Lee et al. 2011). Up to now, rod-to-rod type spark discharge generators (RR-SDG) shown in Fig. 2.1. have been widely studied, and the effects of its parameters have been well defined (Tabrizi et al. 2009a) In addition, it has been recently applied to synthesize bimetallic or mixed metallic nanoparticles synthesis (Byeon et al. 2008a; Tabrizi et al. 2009b; Tabrizi et al. 2010), and to grow nanowires (Messing et al. 2009). A point-to-grid configuration was studied to demonstrate that aerosol production by corona in clean gas at atmospheric pressure was related to the development of plasma filaments reaching the low-field electrode grid in streamer and spark discharge regimes for positive point discharge while aerosol generation occurred only in the spark regime with negative point discharge (Borra et al. 1998). Even though a spark discharge generator (SDG) is known to produce nanometer sized particles, charged aerosols less than 10 nm at high concentrations tend to get agglomerated due to the post-

discharge electrostatic agglomeration of bipolar nanoparticles resulting from post-discharge diffusion charging in bipolar ion clouds, which was studied by measuring post-spark ion density for the RR-SDG (Bau et al. 2010). Prevention of agglomeration and generation of a larger amount of smaller sized charged aerosols from this facile method could further strengthen its advantages and widen the range of applications.

Agglomeration of particles in a SDG could be lessened by controlling some operational parameters such as spark frequency, spark energy and flow rate of a carrier gas over about 10 lpm (Helsper et al. 1993; Schwyn et al. 1988; Tabrizi et al. 2009a). In different systems such as in furnace reactor and flame reactor, ions have been utilized for preventing agglomeration of particles (Nakaso et al. 2003; Jung et al. 2008).

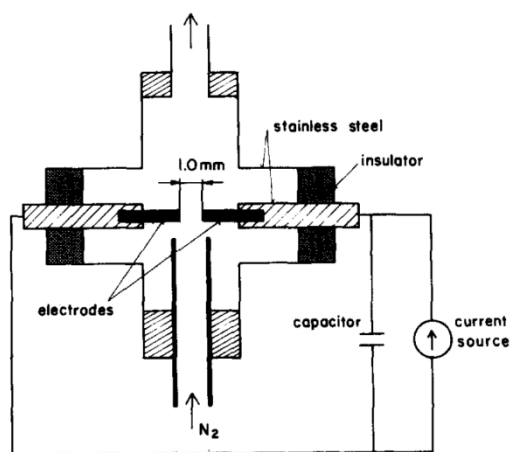


Figure 2.1. A conventional spark discharge generator (Adopted from Schwyn et al. 1988.)

Motivated by these, we attempt to use a pin-to-plate type electrode configuration for generating much smaller and unagglomerated charged aerosols compared to the conventional RR-SDG. The pin-to-plate type spark discharge generator (PP-SDG) has asymmetric electrodes consisting of a pin with a sharp tip as a positive electrode and a grounded plate with a central exit hole. Size and charge distributions of particles for both the PP-SDG and the conventional RR-SDG were measured, and spark parameters and flow pattern for both cases were investigated to explain why the PP-SDG produces much smaller and less agglomerate charged aerosols with a narrower size distribution at higher concentrations than the conventional RR-SDG.

Charged distribution of particles via RR-SDG could be changed with respect to spark frequency. Particle losses to the electrodes and chamber walls have been known to affect charge distribution of as-produced particles. However, characterization for charged distribution of particles via SDGs with respect to spark parameters has been rarely studied. Charge distribution was studied with RR-SDG and investigated with measuring charged particles with respect to spark frequency and the polarity of applied potential. The higher spark frequency in the RR-SDG produced the larger ratio of positively charged particles to negatively charged ones.

2.2. Experimental Concept

2.2.1. Spark discharge

Spark is a transient electrical discharge phenomenon. Electrical discharge regimes are usually divided by dark discharge, glow discharge, and arc discharge, as shown in Fig. 2.2. These regimes could be classified by the value of current and the corresponding voltage lasting during electrical discharge. Current range of the dark discharge, glow discharge and arc discharge correspond to $\sim \mu\text{A}$ with high voltage, $\sim \text{mA}$ with moderate voltage, and above 1 A with relatively low voltages, respectively. The spark discharge with instantaneous current comparable to that of arc discharge could be called current limited arc or transient arc even though the spark is a transient discharge phenomenon different from these discharges. The state of the plasma in the channel of even a very transient spark discharge resembles the state in the arc column, so the spark discharge can be described as a pulsed arc (Raizer 1991). Spark discharge mechanism is normally explained by two discharge concepts. The Townsend model is based on self sustained electron multiplication by secondary electrons generated at an electrode. Paschen's law has been satisfactorily used to estimate the breakdown criteria using the Townsend model. However, Townsend model is difficult to fully explain the discharge with large electrode gap, with the cathode material having very low secondary emission coefficient, and with asymmetric electric field and so on. To explain these discrepancies of Townsend model, a streamer concept was devised by Loeb, Meek and Raether, which is described as a thin ionized

channel between electrodes. The streamer is initiated by an electron avalanche like the Townsend model and then the streamer grows along the positively charged ions left by the initial avalanche. These avalanches are sustained by newly generated electrons close to streamers, and the electrons are produced by photons emitted from atoms excited by the primary and secondary avalanches. In this concept, the photons emitted from the atoms play critical roles in sustaining and growing the streamer. This concept is significantly different from Townsend model sustaining electron multiplication by secondary electrons. The streamer consisting of charges and having the resultant conductivity can connect both electrodes when it reaches the other electrode from one electrode. Consequently, electrical current may be sharply increased, which leads to a spark discharge between the electrodes.

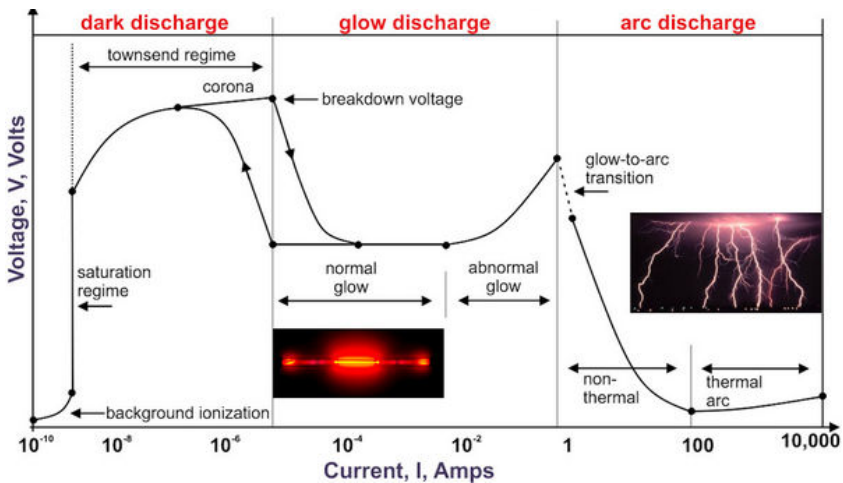


Figure 2.2. Characteristic of Voltage and current during discharge (Adopted from <http://www.plasma-universe.com>)

2.2.2. Pin-to-Plate type spark discharge generator

The schematics of spark discharge chambers with two different electrode configurations used in the experiment; “pin-to-plate configuration” and “rod-to-rod configuration” are depicted in Fig. 2.3. The configuration shown in Fig. 2.3A has asymmetric electrodes and the one shown in Fig. 2.3B has symmetric electrodes as used in a conventional SDG.

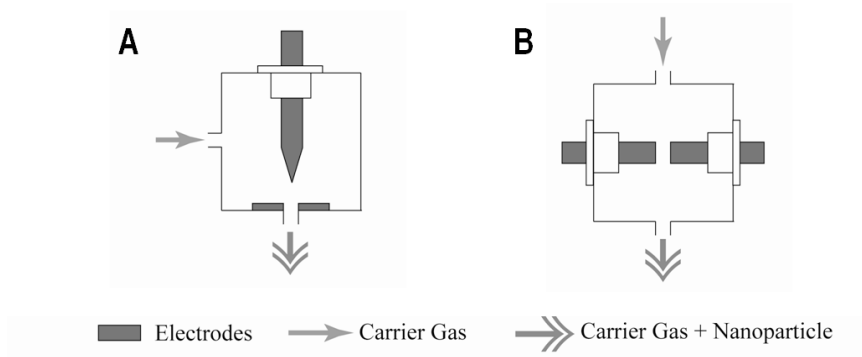


Figure 2.3. Two different configurations of spark discharge generator. (A) pin-to-plate type electrode configuration. (B) rod-to-rod type electrode configuration. (Adopted from Han et al. 2012)

Both generators are composed of a chamber having about 98.2 cm³ in volume with an inner diameter of 5 cm and height of 5 cm. For the pin-to-plate configuration, a pin electrode of diameter of 7mm was made to have a sharp tip with a radius of curvature of approximately 0.13 mm at the end with high positive potential while the grounded plate electrode was made to have an exit hole of 1-mm-diameter in the center. For the rod-to-rod configuration, two cylinders of electrodes having a diameter of 7mm are installed in the middle of the chamber. The electrode holders were precisely machined and assembled to the center position of the chamber to make sure accurate alignment within several micrometer tolerances. In-Sn alloy, silver and copper materials were prepared as electrodes and the gap distance between electrodes was fixed as 2.5 mm for both configurations. Argon gas with a purity of 99.999 % was used as a carrier gas with a fixed flow rate of 3.5 lpm. Generated particles were flowed out through the 1-mm-diameter exit hole for both cases. Experimental conditions were kept constant through all experiments.

2.2.3. Electric circuit for spark discharge

The electric circuit for spark discharge was prepared similar to that widely used in other researches, as shown in Fig. 2.4 (Schwyn et al. 1988; Tabrizi et al. 2009a). The circuit was composed of a high voltage source (HV), an external capacitor (C_{ext}) and a resistor (R_c). Charging current to the capacitor could be controlled by changing resistance of the charging resistor or the applied positive potential of the HV. The HV (Bertan 205B, maximum voltage of 10kV) was connected in serial through the charging resistor of 10 Mohm to the pin electrode for pin-to-plate configuration or one rod electrode for rod-to-rod configuration. The capacitor of 8 nF was connected in parallel to electrode which value is much larger than the intrinsic capacitance of SDGs measured as sub-pico Farad. A high voltage probe (HV probe) and a current probe were installed at positive electrode and a grounded cable, respectively in order to measure spark frequency and discharge current during spark.

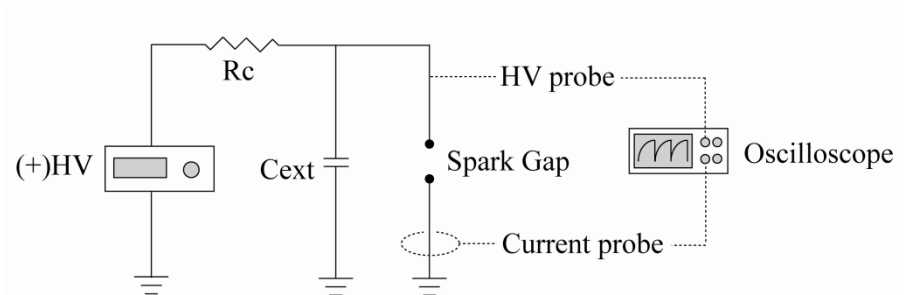


Figure 2.4. Schematic of electric circuit for spark discharge system (Adopted from Han et al. 2012)

2.2.4. Measurement of sizes and charge distribution of particles

The experimental setup for size measurements consists of differential mobility analyzer (DMA), condensation nuclei counter (CNC), Faraday-cup electrometer and electrostatic precipitator (ESP), as shown in Fig. 2.5. Sampled particles for high resolution-transmission electron microscope (HR-TEM, JEOL JEM-3011) measurement were acquired on a TEM grid installed in ESP to observe the morphology and size of nanoparticles. Size distributions of generated particles based on electrical mobility diameter were measured by SMPS system composed of aerosol neutralizer (Kr-85), DMA (DS Industry, Column length of 15cm) and CNC (TSI 3022A). Size measurement for particles smaller than 5 nm was done with high resolution TEM image analysis and represented as projected area equivalent diameters (PAED). Particles were transported directly to DMA and the electrometer without passing through a neutralizer in order to measure currents for estimating the amount of charged aerosols having each polarity. Electrical mobility (Z_p) of particles (Hinds, W. C. 1999) is defined in [Equation 2.1].

$$Z_p = \frac{neC_c}{3\pi\mu d_p} \quad \text{[Equation 2.1]}$$

where n is the number of elementary charges of particles, e is the elementary charge, μ is dynamic viscosity of the carrier gas and d_p is the

particle diameter, and C_c is the slip correction factor or Cunningham correction factor (Li and Chen 2005) defined as [Equation 2.2].

$$C_c = 1 + \frac{\lambda}{d_p} [1.142 + 0.558 \exp(-0.999 \frac{d_p}{2\lambda})] \quad \text{[Equation 2.2]}$$

where μ and λ are dynamic viscosity and mean free path of carrier gas, respectively and d_p is a particle diameter. Electrical mobility could be calculated in term of parameters of DMA as expressed in [equation 2.3].

$$Z_p = \frac{Q_{sh}}{2\pi LV} \ln(R_{outter} / R_{inner}) \quad \text{[Equation 2.3]}$$

where Q_{sh} is the flow rate of sheath gas supplied to DMA, R_{outter} and R_{inner} are the outer radius and inner radius of DMA column, respectively, L is the column length of DMA and V is the voltages applied to inner column of DMA. Voltages applied to DMA could be obtained from relation of [Equation 2.1] and [Equation 2.3] in order to attract particles with the corresponding electrical mobility as follow.

$$V = \frac{3\mu d_p Q_{sh}}{2neC_c L} \ln(R_{outter} / R_{inner}) \quad \text{[Equation 2.4]}$$

Size distribution of aerosols was usually measured with air as a carrier gas using SMPS system. In this experiment, argon was used as the carrier gas. The use of argon as carrier gas has some precaution in SMPS measurement

contrary to the case of air environment. First, dynamic viscosity and mean free path of argon should be considered to calculate electrical mobility because properties of argon are different from those of air. The properties in Table 2.1 were used for mobility calculation. These properties should be set in SMPS before measurement. Secondly, calibration of flow meter in DMA controller supplying sheath flow to DMA should be checked since flow meter usually is calibrated in terms of air environment. In some cases, pump for sheath flow in DMA controller could be severely damaged due to high loading by misleading control signal when it is used without calibration.

Table 2.1. Properties of gases at Standard Conditions: 294.3K, 1 atm (Schmid et al. 2002)

Carrier Gas	Mean free path[m]	Dynamic viscosity[PaS]
Argon	7.07E-8	2.236E-5
Air	6.67E-8	1.82E-5

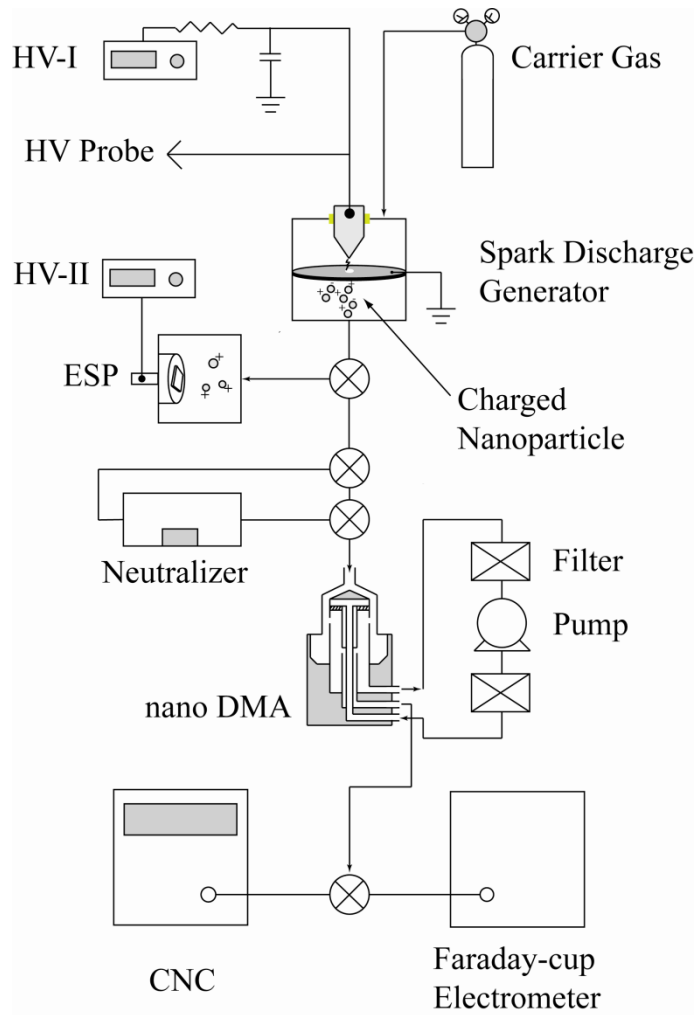


Figure 2.5. Experimental schematic for particle measurement system.

2.3. Results and discussion

2.3.1. Less agglomerated aerosol via Spark Discharge

Figure 2.6 shows morphologies and size distributions of In-Sn alloy particles generated by each configuration with the applied positive potential of 5 kV. For PP-SDG, particles are less agglomerated than for RR-SDG, as shown in Fig. 2.6A and 2.6B. Size distributions were also compared from PAED size distributions based on TEM image analysis in Fig. 2.6C and mobility size distribution based on SMPS measurements in Fig. 2.6D. The geometric mean diameter (d_g) of In-Sn alloy nanoparticles produced via the PP-SDG was found to be much smaller (PAED: 9.2 nm) than that via the RR-SDG (PAED: 13.5 nm), as shown in Fig. 2.6C. In addition, the PP-SDG generated particles having a narrower size distribution (geometric standard deviation, σ_g : 1.36) than that of the RR-SDG (σ_g : 1.79). Mobility size distributions measured by SMPS also shows the same trend in Fig. 2.6D. Another interesting feature for the PP-SDG was that it produced more than twice the number concentrations of particles via the RR-SDG, as shown in Fig. 2.6D.

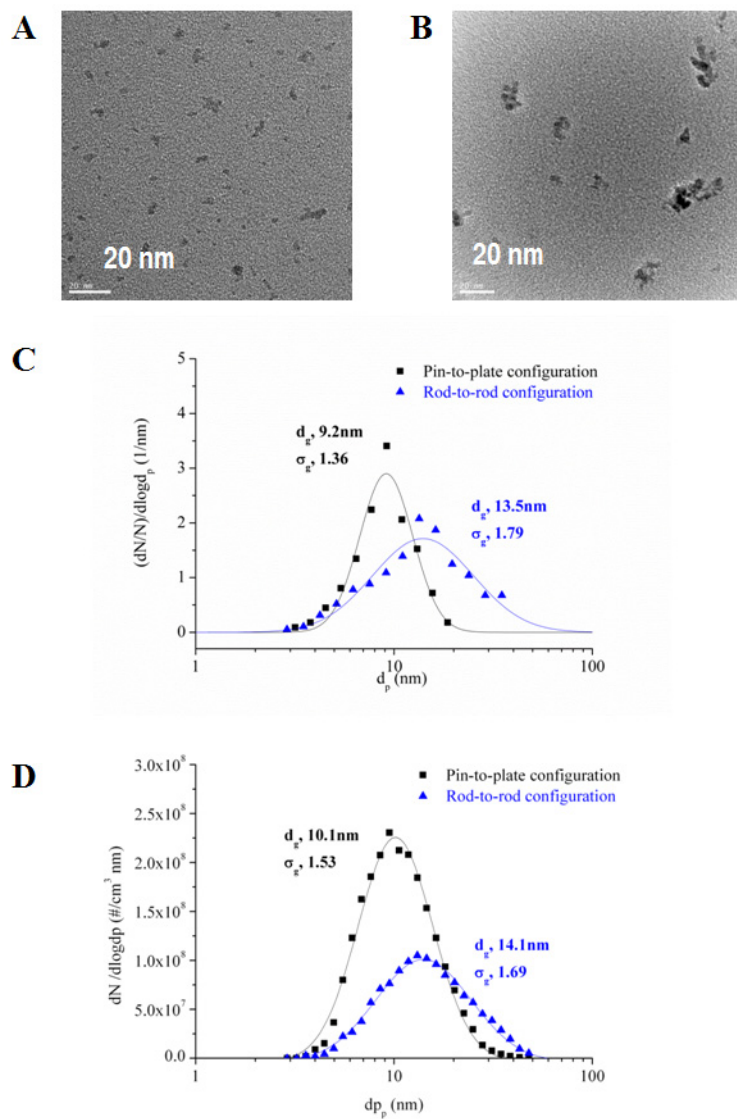


Figure 2.6. In-Sn alloy nanoparticles generated by spark discharge generator with a gap distance of 2.5 mm, argon gas flow rate of 3.5 lpm and applied positive potential of 5 kV. (A) A TEM image of particles for pin-to-plate type SDG. (B) A TEM image of particles for rod-to-rod type SDG (C) PAED based size distributions (D) Mobility diameter based size distributions. (Adopted from Han et al. 2012)

Generations of silver and copper nanoparticles were also examined via two different electrode configurations. Figure 2.7 and 2.8 show TEM images and PAED size distributions of silver and copper nanoparticles synthesized by each configuration with the same experimental conditions used for In-Sn alloy. The same trend of achieving much smaller and unagglomerated nanoparticles was confirmed when the PP-SDG was used, as shown in Fig. 2.7A and 2.7B. TEM analyses for silver and copper particles produced via two different electrode configurations show the generation of unagglomerated and smaller particles via PP-SDG compared to RR-SDG. The size distribution of silver particles with d_g of 5.36 nm and σ_g of 1.37 for pin-to-plate configuration was obtained while conventional rod-to-rod configuration generated much larger nanoparticles with a broader distribution having d_g of 7.19 nm and σ_g of 1.59 according to PAED analysis shown in Fig. 2.7C. The case of copper also demonstrated the same trend of generating smaller and narrower size distribution via PP-SDG as shown in Fig. 2.8A, 2.8B, and 2.8C.

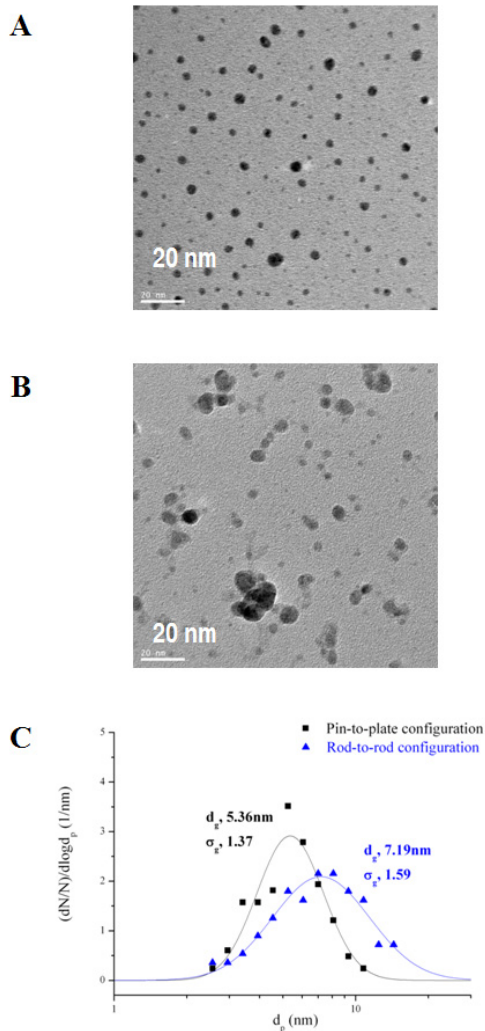


Figure 2.7. Silver and copper nanoparticles generated by spark discharge with a gap distance of 2.5 mm, argon gas flow rate of 3.5 lpm and applied positive potential of 5 kV. (A) A TEM image of silver particles for pin-to-plate type SDG. (B) A TEM image of silver particles for rod-to-rod type SDG. (C) PAED based size distributions of silver particles. (Adopted from Han et al. 2012)

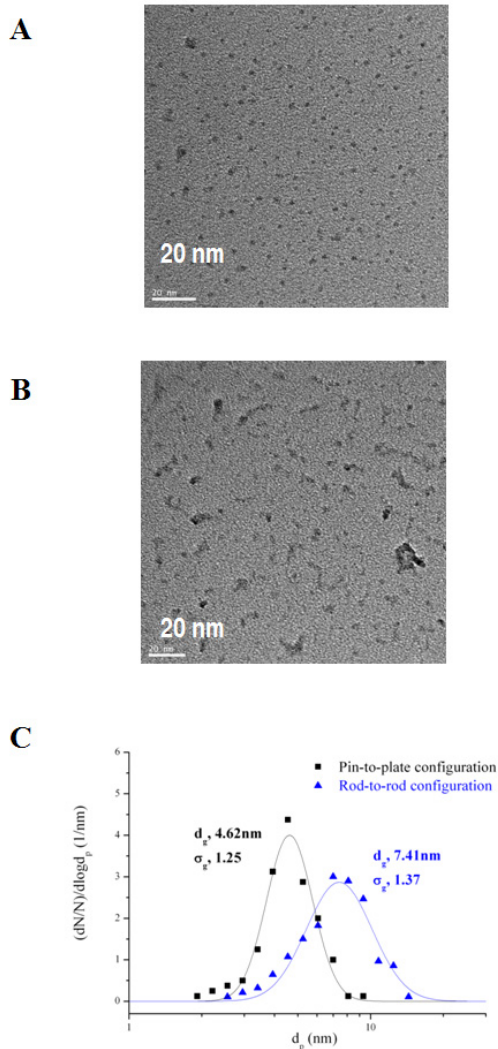


Figure 2.8. Silver and copper nanoparticles generated by spark discharge with a gap distance of 2.5 mm, argon gas flow rate of 3.5 lpm and applied positive potential of 5 kV. (A) A TEM image of copper particles for pin-to-plate type SDG. (B) A TEM image of copper particles for rod-to-rod type SDG. (C) PAED based size distributions of copper particles. (Adopted from Han et al. 2012)

2.3.2. Electrical response during spark discharge

Electrical responses during spark discharge and charge states with respect to electrode configuration were obtained by monitoring voltage and current of the electrical circuit. Fluctuations of voltage and current during spark discharge are shown in Fig. 2.9. Both voltage and current during spark discharge oscillate symmetrically between their positive and negative values and decay within several μ -second.

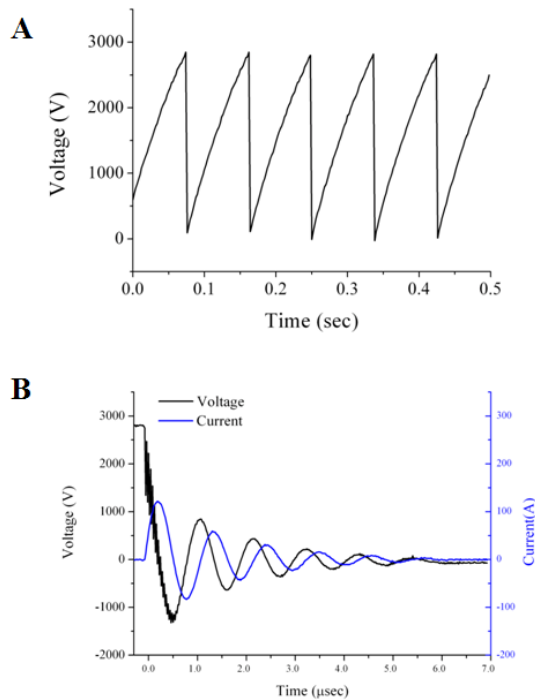


Figure 2.9. Electrical responses during spark discharge. (A) Voltage oscillation with respect to time defining spark frequency (B) Voltage and current oscillation during spark discharge. (Adopted from Han et al. 2012)

2.3.3. Charge distribution of generated particles

The charge distribution of particles was obtained through measurement of the portion of each polarity aerosols generated from two different electrode configurations. Figure 2.10 shows measured current versus electrical mobility for positively and negatively charged particles of In-Sn alloy with applied positive potential of 5 kV. The PP-SDG produced about twice as much as the amounts of charged particles via the RR-SDG. In addition, the number of positively charged particles was approximately the same as that of negatively charged ones while unequal distribution of charged particles was obtained via conventional RR-SDG. Even though PP-SDG could generate unipolar positive ions between sparks, it seems that this could not influence charge distributions of particles significantly, since the faster transport of as-generated particles through the center hole could not allow sufficient time of charging. Contrastively, RR-SDG generated biased charge distributions: more negative particles than positive ones.

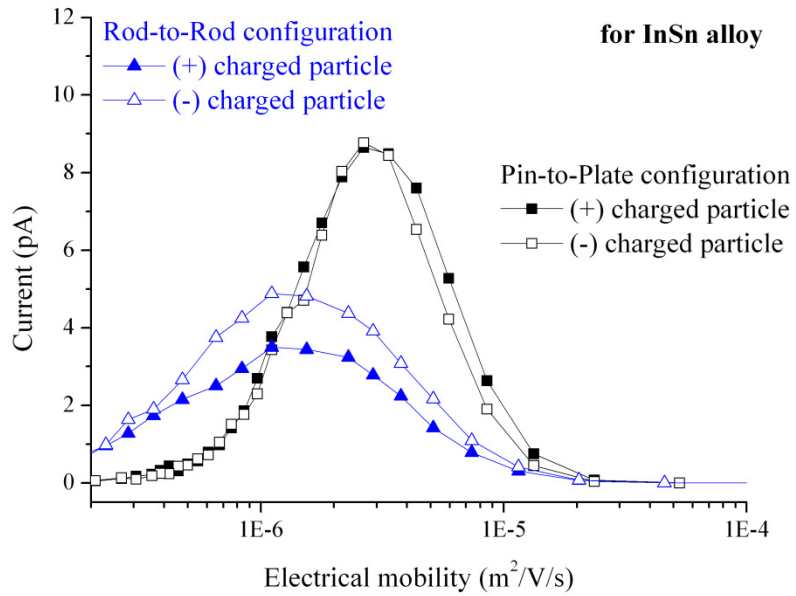


Figure 2.10. Current versus electrical mobility for positively and negatively charged particles of In-Sn alloy for each configuration with a gap distance of 2.5 mm, argon gas flow rate of 3.5 lpm and applied positive potential of 5 kV. (Adopted from Han et al. 2012)

2.3.4. Spark parameter analysis

To explain why the PP-SDG generates much smaller and less-agglomerated nanoparticles with a narrower distribution than conventional RR-SDG, spark frequencies and spark discharge voltages were measured because the spark frequency is known to play an important role determining particle sizes (Tabrizi et al. 2009a). The spark discharge started to occur at the voltage of about 2.8 kV for PP-SDG and at about 2.7 kV for RR-SDG, respectively. Spark energy was calculated by the half of the product of the capacitance and the square of spark discharge voltage (Horvath and Gangl 2003). The spark frequency and spark energy versus applied positive potentials for two different configurations are presented in Fig. 2.11A. The PP-SDG has about 13% lower spark frequency and has about 7 % higher spark energy due to higher discharge voltage compared to the RR-SDG for fixed capacitance, electrode gap and applied potential of 5kV. The reason why the use of pin electrode decreases spark frequency and increases spark discharge voltage could be inferred from electric field analysis. Calculated electrical fields between electrodes by COMSOL software are presented in Fig. 2.11B and inset images describe the calculated equi-potential lines between the electrodes at the breakdown potential of 2.7 kV for the RR-SDG. Breakdown at the potential of 2.7kV with gap distance of 2.5mm for RR-SDG under Argon atmosphere seems to be reasonably compared with other reports (Tabrizi et al. 2009a; Vons, V. et al. 2011). Corresponding electric field strength for breakdown is calculated to be about $1E6$ V/m.

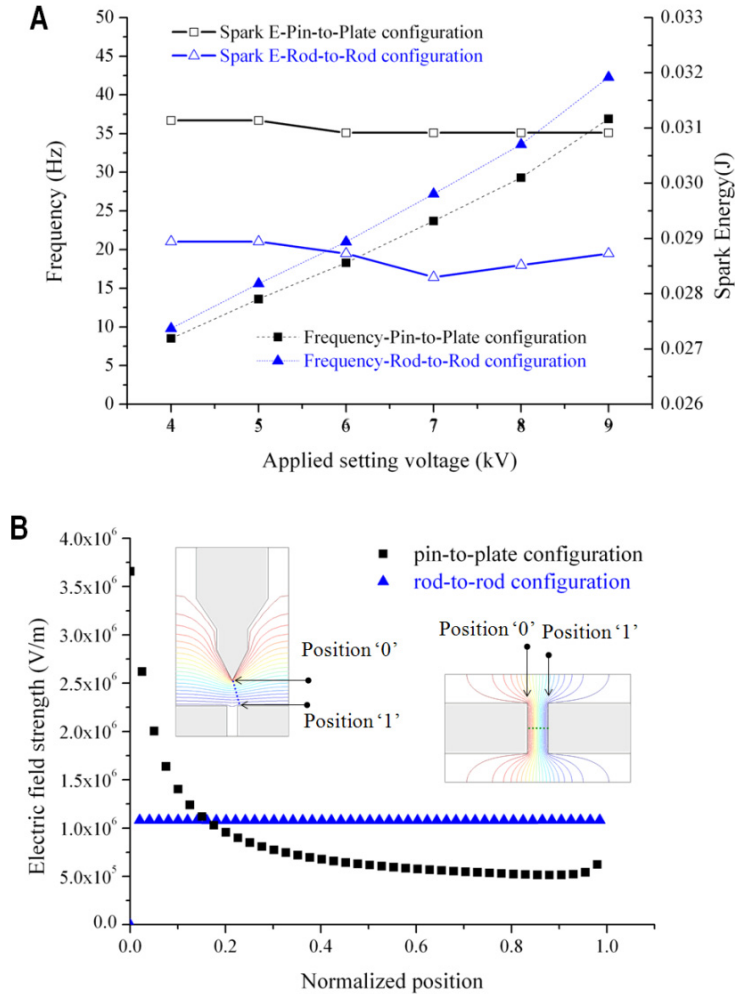


Figure 2.11. Spark parameters and electric field strength for each configuration (A) Spark energy and spark frequency versus applied positive potentials for different configurations (B) the calculated electrical field strength between the gap of electrodes and equipotential lines (insets) between the electrodes along the dashed lines for different configurations with the applied positive potential of 2.7 kV. (Adopted from Han et al. 2012)

Spark discharge in the PP-SDG began to occur at 2.8kV while the calculated electrical field strength near the plate was lower than the breakdown field strength. This discrepancy could be explained by considering space charges and reduced electric field which is defined by electric field divided by the density of neutral species (E/N) (Bau et al. 2010). Space charges including ions and electrons are generated at the end of sharp electrode near the discharge voltage by positive corona and streamers. Streamer can be changed into spark through the increase of reduced electric field caused by enhancement of ionization and the resultant decrease of neutral gases. Thus, the actual breakdown field strength may be lower than the numerically estimated value (Borra, 2006). This analysis explains qualitatively why the PP-SDG requires higher discharge voltage and thereby operates lower spark frequencies for the given applied positive potential compared to the RR-SDG. In addition, the radius of the curvature of the pin electrode could affect the electric field strength between the electrodes as shown in Fig. 2.12. However, the spark energy and spark period (inverse of spark frequency) are expected to decrease as the radius of curvature of pin electrode increases since the pin electrode having large radius of curvature behaves like a rod electrode. The effect of sharpness of pin electrode is hard to conclude because the sharper pin electrode has both higher spark energy and lower spark frequency under fixed applied setting potential in comparison to more blunted pin electrode. Difference in spark frequency and in its inversely proportional spark energy cannot explain fully the observed significant reduction of particle size and the phenomenon

of unagglomeration.

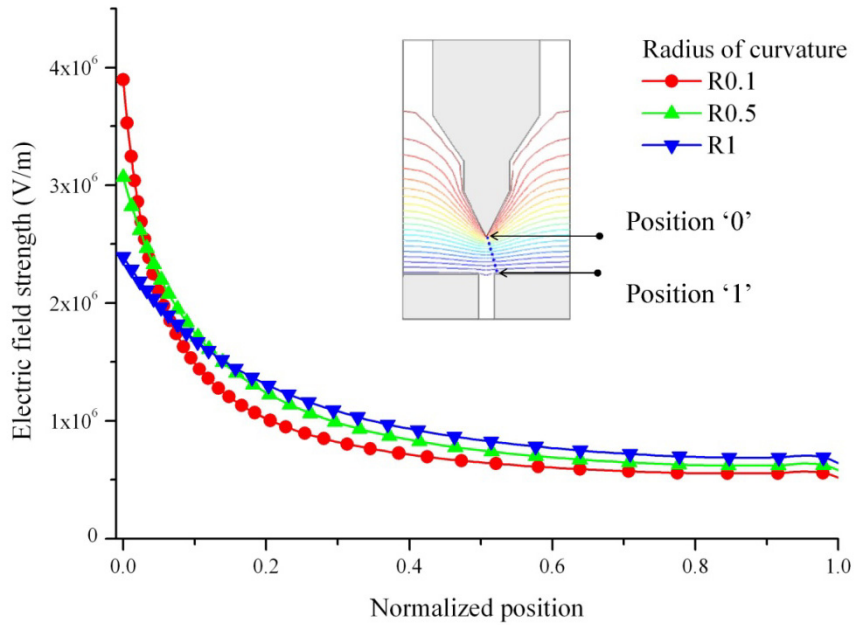


Figure 2.12. The calculated electrical field strength between the electrodes with respect to the radius of curvature of pin electrode for pin-to-plate electrode with the same condition as Fig. 2.11B

2.3.5. Flow pattern in spark discharge generators

Flow patterns should be significantly different for PP-SDG and RR-SDG due to totally different electrode geometry, i.e. transverse flow exists between electrode gap of RR-SDG and axial flow is dominant between gap of PP-SDG. Flow patterns both in PP and RR spark discharge generators (SDG) were studied using 3D model of commercial software, COMSOL and found to be very important. Red colored is the region of high velocity exceeding 3 m/sec. The calculations show that the PP-SDG has much higher gas velocity near particle generation zone and thus much faster transport of as-generated particles as shown in Fig. 2.13A than for the case of RR-SDG shown in Fig. 2.13B. This much faster transport of generated particles in the PP-SDG could reduce coagulation probability explaining both the generation of smaller sizes and less agglomeration than the case of the RR-SDG.

To find out whether the use of a pin electrode or flow pattern plays more dominant role on the reduction of coagulation probability for pin-to-plate type chamber, we studied an additional case of Pin to Rod (PR) type chamber in which one of the rods of the conventional RR-SDG was replaced by a pin electrode, as shown in Fig. 2.14A. The PR-SDG is expected to have the same characteristics of ion generation as the PP-SDG due to the use of the pin electrode while the flow pattern and resultant residence time would be similar to that of the RR-SDG. As shown in Fig. 2.14B, both the PR-SDG and the PP-SDG generated higher concentration of charged aerosols than the RR-SDG.

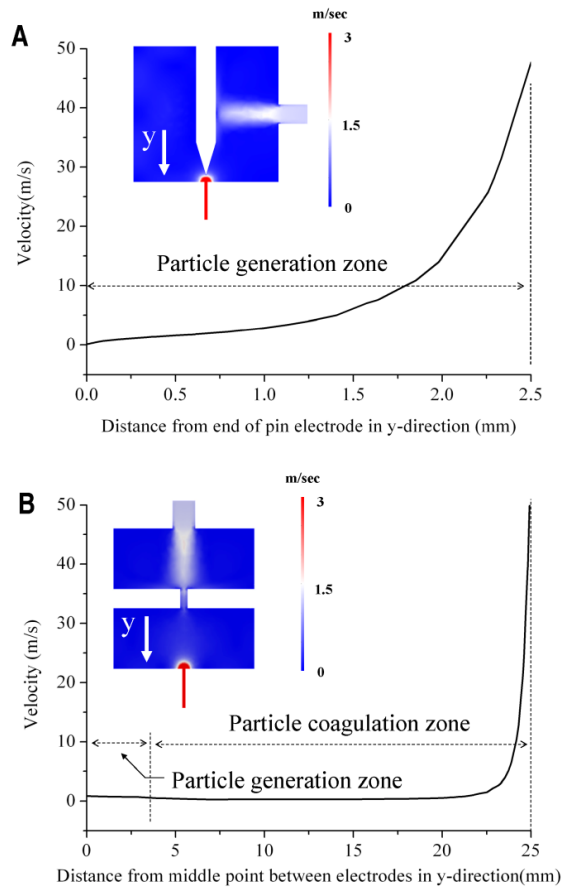


Figure 2.13 Flow fields near particle generation and coagulation zone for each configuration. Insets show colour plots of velocities up to 3 m/s emphasizing high velocities (red colour) between electrode gap of PP-SDG and low velocities (blue colour) between electrode gap of RR-SDG (A) Velocity and its contour in cross-sectional view (inset) near particle generation zone for pin-to-plate configuration. (B) Velocity and its contour in cross-sectional view (inset) near particle generation and coagulation zone for rod-to-rod configuration. (Adopted from Han et al. 2012)

It is clear that the use of the sharp pin electrode for both the PR-SDG and the PP-SDG could generate higher concentration of charged aerosols than the RR-SDG.

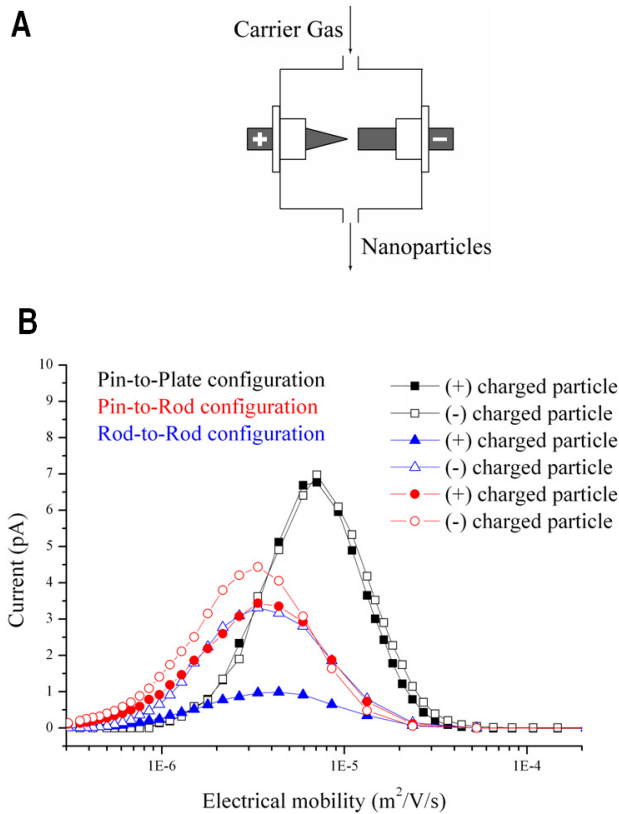


Figure 2.14. Pin-to-Rod type electrode configuration and charged particle generation during spark discharge with silver. (A) Pin-to-rod type electrode configuration. (B) Current versus electrical mobility for positively and negatively charged particles of silver for three different types of configuration with a gap distance of 2.5 mm, argon gas flow rate of 3.5 lpm and applied positive potential of 5 kV. (Adopted from Han et al. 2012)

It is interesting to note that the PR-SDG having similar flow residence time to the RR-SDG generated similar sized particles to the RR-SDG, but much larger sizes than PP-SDG. This means that the flow pattern difference in our experiments played more dominant role on the determination of particle sizes than the difference in charged aerosol generations with sharp pin electrode.

The faster transport of charged particles in the PP-SDG resulted in nearly equal charge distribution of particles while the slower transport of the RR-SDG caused unequal distribution of charged particles. Similar biased charged aerosols were previously reported in the conventional RR-SDG (Tabrizi et al. 2009a) and authors explained this by the loss of positive particles on the wall. Fast transport of charged aerosols in the PP-SDG could not only prevent the particle deposition on the electrodes and chamber wall, but reduce the probability of post-discharge neutralization process, which could result in almost equal polarity aerosols. The slow transport in the RR-SDG allows sufficient time for both wall loss and post-discharge neutralization process shown in Fig. 2.15A by bipolar ion clouds resulting in asymmetric charge distribution due to the difference in mobility of positive and negative ions as shown in Fig. 2.15B (Wiedensohler, A. and Fissan, H., 1991). Even for the case of PR-SDG, negative aerosol biased charge distribution was obtained due to having a similar flow residence time to the case of RR-SDG while the use of sharp pin electrode apparently generated more charged aerosols.

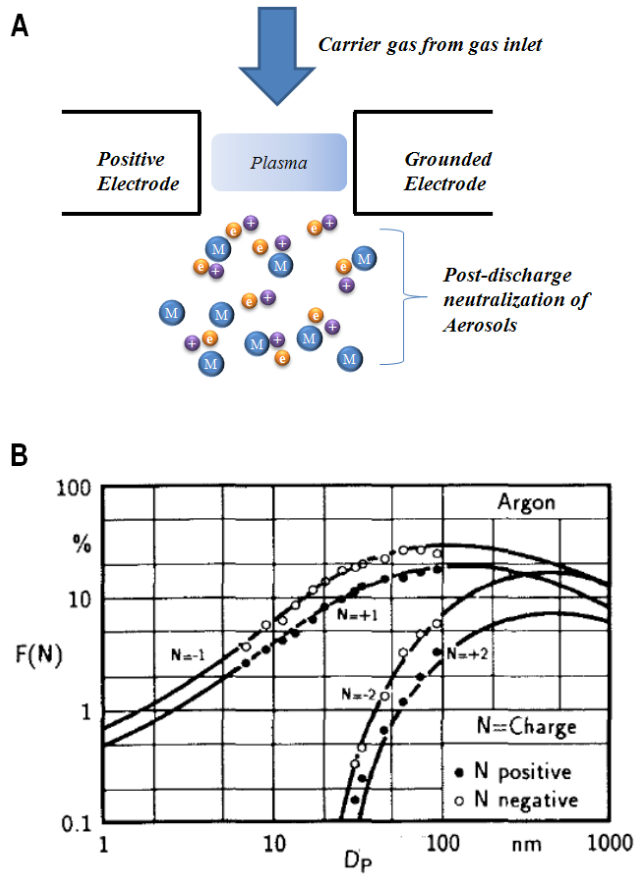


Figure 2.15. Post-discharge neutralization in RR-SDG (A) The schematic of post-discharge neutralization by ions in slow transport zone in RR-SDG (B) The experimentally determined bipolar charge distribution of aerosol particles in argon (Adoped from Wiedensohler, A. and Fissan, H., 1991).

2.3.6. Change in charge distribution of particles.

Interestingly, change in charge distribution of particles generated via the RR-SDG was observed with respect to spark frequency as well as the electrode configuration in SDGs as mentioned before. Negatively charged particles were prevailing in the RR-SDG in the experiment, which was due to the fact that as-generated particles deposited the chamber wall and experienced post-discharge neutralization in the slow transport region. Change in charge distribution of generated particles with respect to spark frequency can infer existence of another factor or loss mechanism affecting the distribution besides well-known factors such as wall loss and the post-discharge neutralization for generated particles. Figure 2.16A shows the charge distribution of particles with respect to spark frequency for the RR-SDG. The ratio of number concentration of negatively charged particles and positively charged particles decreases in the RR-SDG as spark frequency increases as shown in Fig. 2.16B. The rate of increase in generation of positively charged particles grows rapidly as frequency increases, which is assumed to be due to that quantity of electro-deposition of as-generated particles on the surface of the electrodes is changed with respect to spark frequency. Especially, change in the charge distribution in the RR-SDG is thought to be heavily affected by electro-deposition of negatively charged particles because the PP-SDG shows symmetric charge distribution.

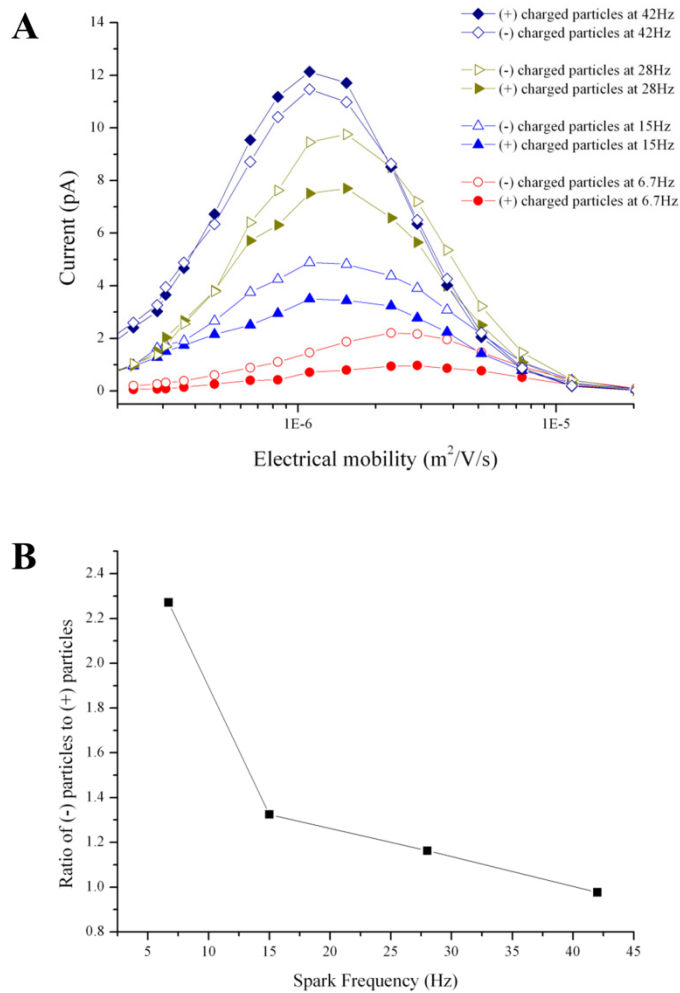


Figure 2.16. Change in charge distribution of particles via the RR-SDG with InSn alloy with respect to spark frequency (A) Charge distribution of particles with respect to spark frequency with a gap distance of 2.5 mm, argon gas flow rate of 3.5 lpm and applied positive potential of 5 kV (B) Change in the ratio of number concentration of negatively charged particles and that of positively charged particles with respect to spark frequency.

Electro-deposition of negatively charged particles could be increased if the potential of positive electrode increases with growing spark frequency during spark discharge. Figure 2.17A shows the measured profiles of voltage and current during spark discharge in milli-second (msec) scale. In the voltage and current curve, the current flowing between the gap of electrodes lasts for about 3 msec, which means that the plasma during spark discharge is maintained for about 3 msec after energetic spark discharge in several micro-second (μsec). Plasma duration time for spark discharge is defined as spark relaxation time (τ_s) hereafter. In addition, the potential of the positive electrode is proportional to spark frequency at the given spark relaxation time, as shown in Fig. 2.17B. The plasma shows electrically conductivity and quasi-neutrality, which resembles a conductor and could screens electric field like a metal because plasma consists of ions, electrons and neutrals, and amount of those charges in plasma is known to be equal. Even a little increase in the potential of the positive electrode causes the strong electric field (E_s) for the gap not between both electrodes but between the electrode and the plasma because the plasma screens the existence of the grounded electrode and the gap between the electrode and plasma could be defined as very thin Debye length of $10^{-3} \sim 10^{-4}$ mm. Positive electric field forms between the positive electrode and plasma with gap of Debye length scale although the plasma itself has a little positive potential due to fast mobility of electrons. The positive electric field causes negatively charged particles to move to the positive electrode and electro-deposition occurs in the electrode.

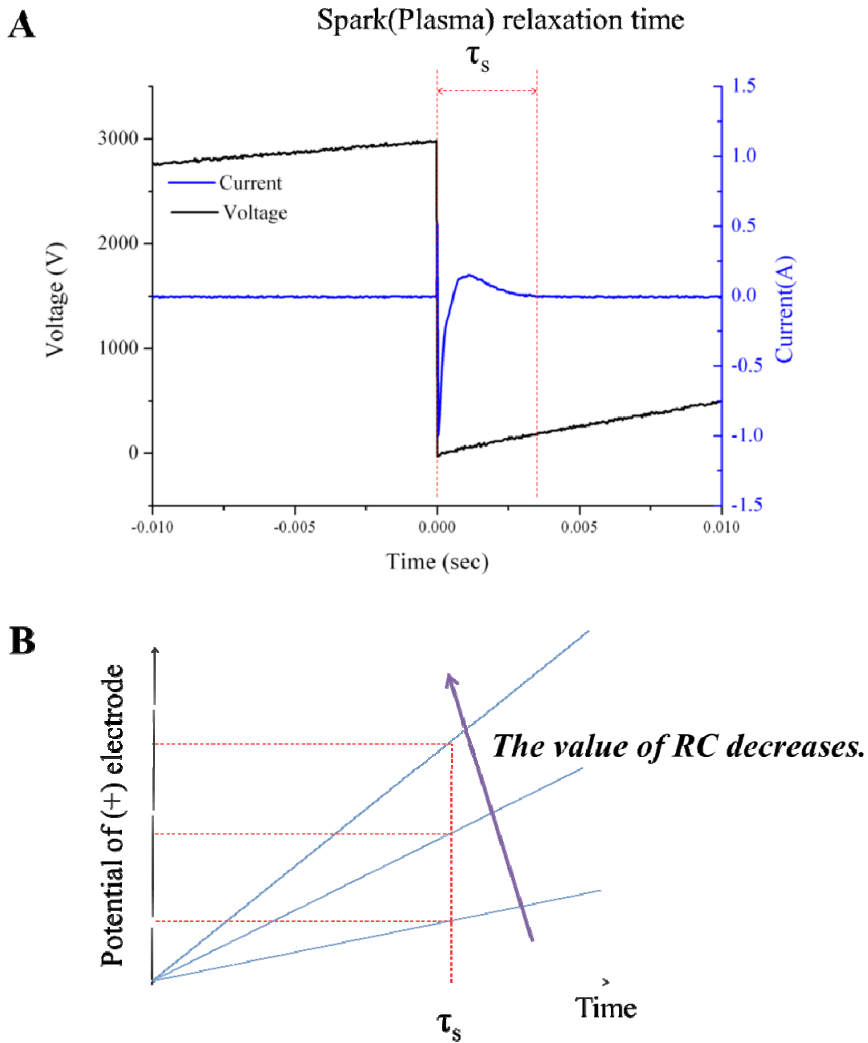


Figure 2.17. Characteristic of voltage and current during spark discharge and change in potential of the positive electrode. (A) Profiles of voltage and current with millisecond scale in SDGs. (B) Increase of potential of positive electrode at spark relaxation time.

The amount of deposition of positive particles to the grounded electrode is kept constant, while amount of negatively charged particles deposited on the positive electrode grows with spark frequency. Electro-deposition of negatively charged particles becomes comparable to that of positively charged particles as the spark discharge increases. For that reason, the symmetric charge distribution of the particles in the RR-SDG is observed at the spark discharge of 42 Hz as shown in Fig. 2.16. Therefore, negatively charged particles become dominant at lower spark frequency while positively charged particles become prevailing among charged particles at higher frequency. This is due to the fact that the relatively strong resultant field with higher spark frequency could attract much more negatively charged particles to the positive electrode efficiently during the given spark relaxation time in the RR-SDG compared to the cases of lower spark frequency.

Electric field (E_s) between positive electrode and plasma could be obtained from the potential ($V_{\text{electrode}}$) of the electrode divided by the Debye length of the plasma ($d_0 = d_A$ or d_C) in [Equation 2.5].

$$E_s = \frac{V_p}{d_0} \quad \text{[Equation 2.5]}$$

$$V_{\text{electrode}} = V_{HV} (1 - \exp(-t/RC)) \quad \text{[Equation 2.6]}$$

The potential of the positive electrode in the RC circuit is defined as [Equation 2.6] and the equation could be simplified to [Equation 2.7] according to Taylor series.

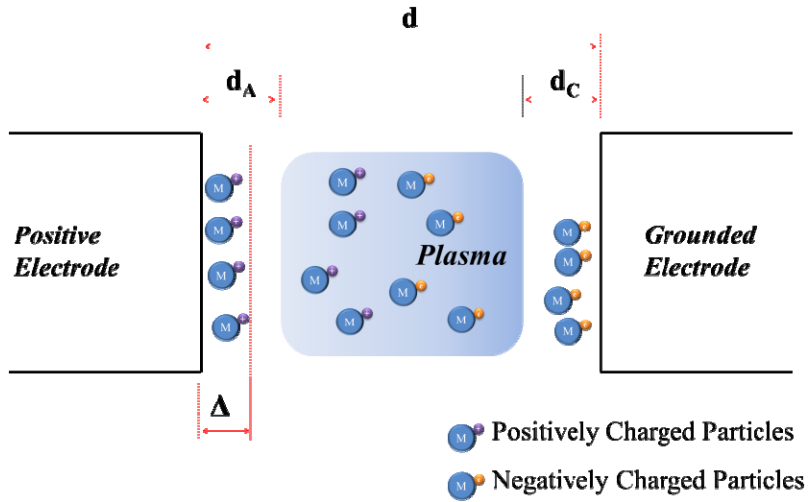


Figure 2.18. Schematic of electro-deposition of charged particles in a plasma on the electrodes during spark discharge.

The electric field between the positive electrode and the plasma is calculated by [Equation 2.8]

$$V_{electrode} = V_{HV} \frac{t}{RC} \quad \text{[Equation 2.7]}$$

$$E_s = \frac{V_p}{d_0} = \frac{V_{HV}}{d_0} \frac{t}{RC} = \frac{E_0}{RC} t \quad \text{[Equation 2.8]}$$

The arriving times (τ_p) for charged particles having electrical mobility (μ_p) and placing at the distance (Δ) from the positive electrode to reach the electrode at given electric field could be expressed in terms of the relation of the velocity of particles (v_p) and electrical mobility under the specific electric field as expressed in [Equation 2.9].

$$\tau_p = \frac{\Delta}{v_p} = \frac{\Delta}{\mu_p E_s} = \frac{\Delta}{\mu_p \frac{E_0 \tau_p}{RC}} \quad \text{[Equation 2.9]}$$

The time for the charged particles arriving to the electrode could be affected by the product of resistance and capacitance (RC) in the spark discharge circuit. Change in the value of RC means alteration of spark frequency.

$$\tau_p^2 = \frac{\Delta}{\mu_p E_0} RC \Rightarrow \tau_p = \sqrt{\frac{\Delta}{\mu_p E_0} RC} \quad \text{[Equation 2.10]}$$

The arriving time of the charged particles to the electrode increases with square root as the value of RC or the inversion of the corresponding spark frequency increases in [Equation 3.10]. The longer arriving time for the negatively charged particles to reach the positive electrode means that less amount of negatively charged particles are deposited to electrode through the spark relaxation time of about 3 msec. According to this principle, figure 2.19A shows that higher capacitance causes the particles placing further from the electrode to reach the positive electrode. Also, figure 2.19B indicates that the increase of the electrical mobility of particles decreases the arriving time of particles, which means that smaller particles with larger electrical mobility could be easy to be deposited on the surface of the electrode for spark plasma duration time of about 3 msec.

We changed the polarity of HV source from positive potential to negative one in order to confirm the characteristics for electro-deposition of charged particles in the SDG, as shown in Fig. 2.20.

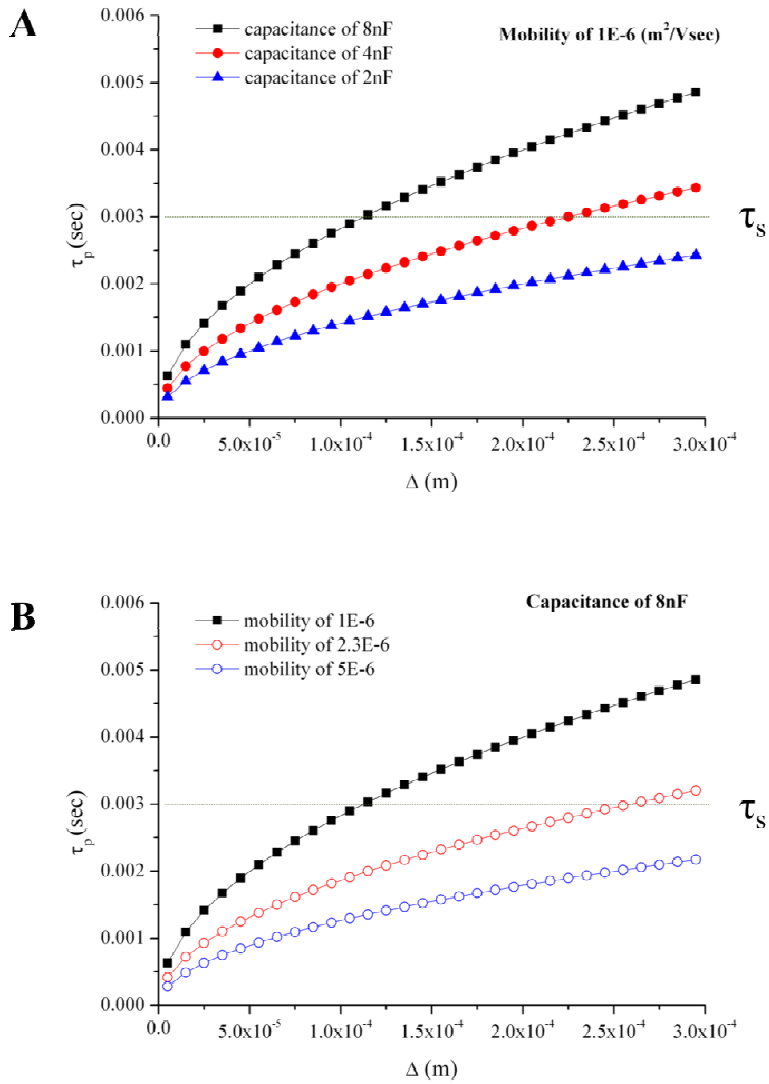


Figure 2.19. Characteristic of electro-deposition of charged particles. (A) Electro-deposition of the charged particles with respect to the capacitance in the spark circuit. (B) Electro-deposition of the charged particles with respect to the mobility of the charged particles. (Assume $E_0 = 1E6$ V/m)

For negative spark discharge in RR-SDG, the amount of negatively charged particles overwhelmed that of positively charged particles with similar frequency in comparison to the cases of positive spark in the RR-SDG. This shows that negative charge distribution of particles becomes prevailing because electro-deposition for positively charged particles becomes more dominant than that for negatively charged particles in the negative RR-SDG. Charge distribution of particles via RR-SDG could be subject to change with respect to spark frequency and thus generation rate of charged particles is not simple relation between spark frequency and production rate while charged particles via PP-SDG are generated with approximately equal number regardless of spark frequency.

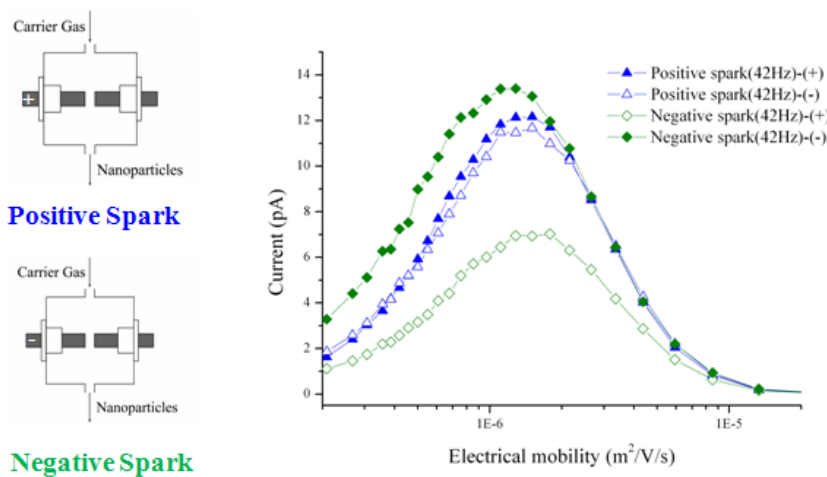


Figure 2.20. Charge distribution of particles via RR-SDG with InSn alloy with respect to electrical polarity with a gap distance of 2.5 mm, argon gas flow rate of 3.5 lpm and applied positive potential of 5 kV.

PP-SDG with InSn alloy produced nearly equal number of charged particles with respect to spark frequency up to about 13Hz, as shown in Fig. 2.21. We changed the capacitance of the capacitor from 8 nF to 2 nF in the circuit to drive the spark with frequency of about 60 Hz and to adjust amount of charged particles within the limit (13 pA) of electrometer. Charge distribution from the PP-SDG with high spark frequency of 60Hz also shows the same trend as PP-SDG with spark frequency of about 13 Hz shown in Fig. 2.10. The change in charge distribution of particles in SDGs is believed to be affected by the characteristic of particle transport.

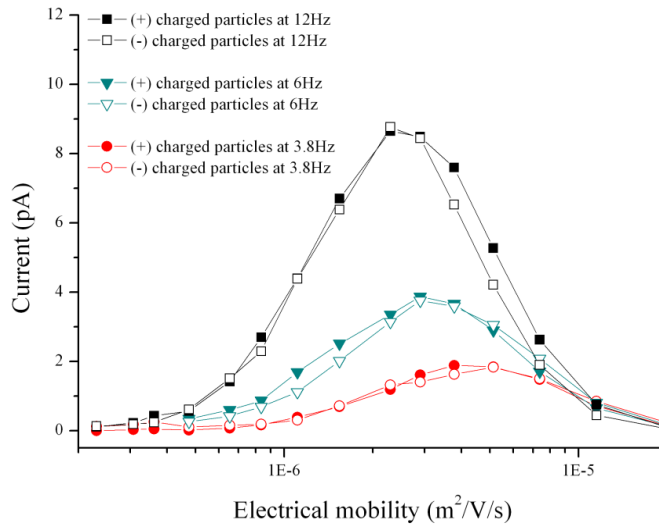


Figure 2.21. Charge distribution of particles via PP-SDG with InSn alloy with respect to electrical polarity with a gap distance of 2.5 mm, argon gas flow rate of 3.5 lpm and applied positive potential of 5 kV.

2.4. Conclusion

We demonstrated that the pin-to-plate type spark discharge generator could produce much smaller unagglomerated charged metal aerosols with a narrower size distribution at higher concentration in comparison to the conventional rod-to-rod type generators. We examined and compared the sizes and charge distributions of particles for In-Sn alloy, silver and copper, and investigated spark parameters and flow pattern for each configuration to explain the observed phenomena. Much faster transport of as-generated particles in the use of pin-to-plate type electrode configuration could explain why smaller and unagglomerated charged aerosols are produced in comparison to the rod-to-rod type generator. The use of a sharp pin electrode resulted in much higher concentrations of charged aerosols.

Charge distribution of generated particles via SDGs was changed with respect to spark frequency in rod-to-rod type generator because electro-deposition of charged particles onto the positive electrode became dominant during spark discharge. In contrast, similar charged distribution of particles for each polarity via pin-to-plate type spark discharge generator was obtained. This is believed that losses of charged particles to electrodes could change with the potential of electrode within plasma duration time with respect to spark frequency. Characteristics of the charge distribution with respect to spark frequency could be also affected by transport of particles by carrier gas as the case of the PP-SDG.

2.5. References

- Bau, S., Witschger, O., Gensdarmes, F., Thomas, D. and Borra, J. (2010). Electrical properties of airborne nanoparticles produced by a commercial spark-discharge generator. *Journal of Nanoparticle Research*, 1-7.
- Biskos, G., Vons, V., Yurteri, C. and Schmidt-Ott, A. (2008). Generation and sizing of particles for aerosol-based nanotechnology. *KONA Powder Particle J*, 26, 13-35.
- Borra, J. (2006). Nucleation and aerosol processing in atmospheric pressure electrical discharges: powders production, coatings and filtration. *Journal of Physics D: Applied Physics*, 39, R19.
- Borra, J., Goldman, A., Goldman, M. and Boulaud, D. (1998). Electrical discharge regimes and aerosol production in point-to-plane DC high-pressure cold plasmas:: aerosol production by electrical discharges. *Journal of Aerosol Science*, 29, 661-674.
- Byeon, J., Park, J. and Hwang, J. (2008). Spark generation of monometallic and bimetallic aerosol nanoparticles. *Journal of Aerosol Science*, 39, 888-896.
- Han, K., Kim, W., Yu, J., Lee, J, Lee, H., Woo, C., and Choi, M. (2012). A study of Pin-to-Plate type spark discharge generator for producing unagglomerated nanoaerosols. *Journal of Aerosol Science*, Accepted.
- Helsper, C., Molter, W., Loffler, F., Wadenpohl, C., Kaufmann, S. and Wenninger, G. (1993). Investigations of a new aerosol generator for the production of carbon aggregate particles. *Atmospheric Environment. Part A*.

General Topics, 27, 1271-1275.

Horvath, H. and Gangl, M. (2003). A low-voltage spark generator for production of carbon particles. *Journal of Aerosol Science*, 34, 1581-1588.

Jung, J., Kim, S. and Kim, S. (2008). Nanoparticle generation using corona discharge ions from a supersonic flow in low pressure. *Powder Technology*, 185, 58-66.

Kim, H., Kim, J., Yang, H., Suh, J., Kim, T., Han, B., Kim, S., Kim, D., Pikhitsa, P. and Choi, M. (2006). Parallel patterning of nanoparticles via electrodynamic focusing of charged aerosols. *Nature Nanotechnology*, 1, 117-121.

Krinke, T. J., Deppert, K., Magnusson, M. H., Schmidt, F. and Fissan, H. (2002). Microscopic aspects of the deposition of nanoparticles from the gas phase. *Journal of Aerosol Science*, 33, 1341-1359.

Kruis, F., Fissan, H. and Peled, A. (1998). Synthesis of nanoparticles in the gas phase for electronic, optical and magnetic applications--a review. *Journal of Aerosol Science*, 29, 511-535.

Lee, H., You, S., Pikhitsa, P. V., Kim, J., Kwon, S., Woo, C. G. and Choi, M. (2011). Three-Dimensional Assembly of Nanoparticles from Charged Aerosols. *Nano Letters*, 11, 119-124.

Messing, M., Dick, K., Wallenberg, L. and Deppert, K. (2009). Generation of size-selected gold nanoparticles by spark discharge--for growth of epitaxial nanowires. *Gold Bulletin*, 42, 20-26.

Nakaso, K., Han, B., Ahn, K., Choi, M. and Okuyama, K. (2003). Synthesis of non-agglomerated nanoparticles by an electrospray assisted chemical vapor

- deposition (ES-CVD) method. *Journal of Aerosol Science*, 34, 869-881.
- Raizer, Y. P. Gas Discharge Physics, 1991, Springer-Verlag.
- Schwyn, S., Garwin, E. and Schmidt-Ott, A. (1988). Aerosol generation by spark discharge. *Journal of Aerosol Science*, 19, 639-642.
- Tabrizi, N., Ullmann, M., Vons, V., Lafont, U. and Schmidt-Ott, A. (2009a). Generation of nanoparticles by spark discharge. *Journal of Nanoparticle Research*, 11, 315-332.
- Tabrizi, N., Xu, Q., Van Der Pers, N., Lafont, U. and Schmidt-Ott, A. (2009b). Synthesis of mixed metallic nanoparticles by spark discharge. *Journal of Nanoparticle Research*, 11, 1209-1218.
- Tabrizi, N., Xu, Q., van der Pers, N. and Schmidt-Ott, A. (2010). Generation of mixed metallic nanoparticles from immiscible metals by spark discharge. *Journal of Nanoparticle Research*, 12, 247-259.
- Vons, V., de Smet, L., Munao, D., Evirgen, A., Kelder, E. and Schmidt-Ott, A. (2011). Silicon nanoparticles produced by spark discharge. *Journal of Nanoparticle Research*, 13, 4867-4879.
- Wiedensohler, A. and Fissan, H. (1991). Bipolar charge distributions of aerosol particles in high-purity argon and nitrogen. *Aerosol Science and Technology*, 14, 358-364.
- Yu, J. (2009). Size control of nanoparticles via different configuration of spark discharge chamber, Master thesis in Seoul National University.

Chapter 3.

Focused Patterning of Charged Nanoparticles on a Non-Conducting Substrate

3.1. Introduction

Establishment of the method to form an ordered array of nanoparticles could enhance practical uses of them as building blocks. Bottom-up patterning using these particles could be a promising alternative to conventional top-down patterning represented by photolithography. Electrostatic force has been widely used for the bottom-up patterning of nanoparticles, which controls the trajectories of the particles, and guides them on desired positions. (Kim et al. 2006; Krinke et al. 2002; Krinke et al. 2001) Patterning by electrostatic force should be accompanied with charged particles.

Charged nanoparticles have been patterned through charge stamping or scrubbing the non-conducting surface, which have been based on charge transfer on the surface of a non-conducting substrate (Deppert 2002). However, these patterning methods have limitation of amount of charged particles to deposit on predefined surface charges on the substrate. Ion-Assisted Aerosol Lithography (IAAL) of nanoparticles was previously reported, as shown in Fig. 3.1 and versatile particle patterning and their applications via the method have been shown (Kim et al. 2006; Lee et al. 2010; You et al. 2010). Accumulation of charged particles at the desired positions on conducting substrates bears a multi-scale structure composed of the particles along electric field lines via the method. The IAAL method has been applicable only on conducting substrates such as highly doped silicon

wafers or metal coated substrates. This is due to that those substrates supply electrical path for charges to escape from the particles and charged particles are attracted with the strong electric field between the substrates and a grounded housing. This principle was not directly applicable to non-conducting substrates. Firstly, thick non-conducting substrates tend to reduce the electric field, which is not easy to obtain the electric field similar to the case of conducting, as shown in Fig. 3.2. Secondly, neutralization of charged particles and the resultant suppression of Coulombic repulsion between the particles is needed for focused patterning of charged particles on non-conducting substrates. These are the reason why patterning of charged particles on a non-conducting substrate is challenging.

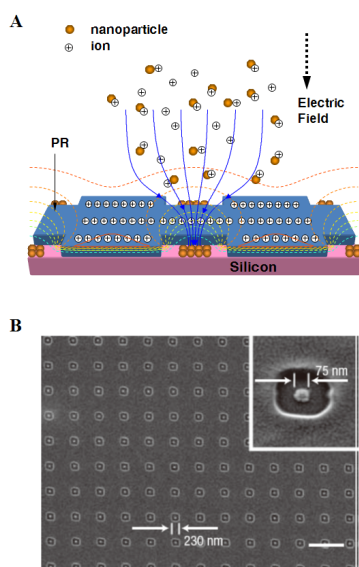


Figure 3.1. Ion-Assisted Aerosol Lithography. (A) Schematic of the principle of IAAL (B) SEM image of patterns via IAAL (Adopted from Kim et al. 2006).

We devised a temporary conducting path to neutralize the charges from deposited charged particles using conductive liquid. The temporary conducting path was realized forming conductive liquid film on the surface of the substrate, which needed conducting liquid droplets and hydrophilic characteristic of the surface. A surfactant was used to modify hydrophilicity of the surface and conducting liquid droplets were supplied via electrospray. The utilization of these factors enables focused patterning of charged particles on non-conducting substrates similar to the case of conducting substrates. Patterns consisting of PSL particles were obtained with nano and micro scale on thick glass and flexible polymer substrates via this method, and several micro-sized conducting wires were patterned with silver nanoinks on the polymer substrates. Spark generated gold nanoparticles and liquid droplets were utilized simultaneously to form sub-micro scaled patterns on the polymer film.

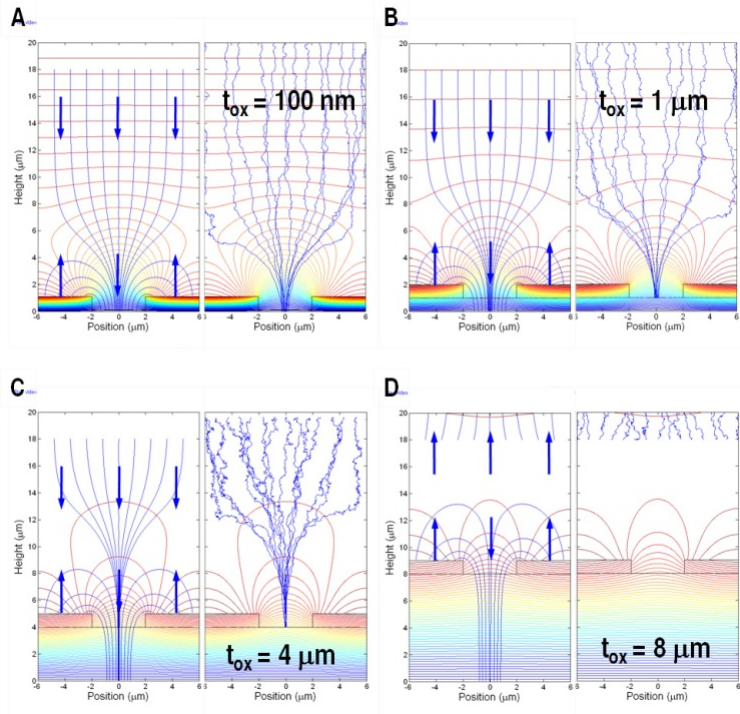


Figure 3.2. Limitation of IAAL method with respect to dielectric thickness on a conducting substrate. (A-C) the Focusing effect of IAAL increases as dielectric thickness on a conducting substrate increases. (D) Distortion of electric field line with 8 μm thick dielectric destroys ion induced focusing lens and nanoparticles are no longer deposited on the substrate. (Adopted from You et al.).

3.2. Experimental Concepts

3.2.1. Focused Patterning of charged particles on a non-conducting substrate

It is a challenging task to pattern charged nanoparticles on thick non-conducting substrates via ion-induced focusing approach. Formation of a conducting path on non-conducting substrates is needed to solve the limitation of IAAL. Formation of conducting path for charged particles is a prerequisite for patterning on a non-conducting substrate. We formed a conducting liquid film on the surface of non-conducting substrates to make the surface conductive during deposition process as shown in Fig. 3.3.

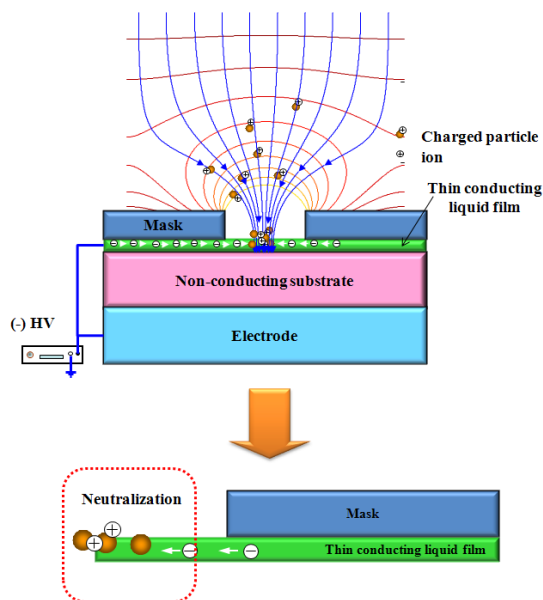


Figure 3.3. Schematic of focused patterning of charged particles on a non-conducting substrate. (Adopted from You et al. 2010).

Formation of a temporary conducting path on a non-conducting substrate was realized by introduction of droplets of conducting liquid. The liquid film is responsible for forming the electric field comparable to the case of conducting substrates and neutralization of charges of the particles, which enables focused pattern on the non-conducting substrate with IAAL principle. Such conducting liquid film was evaporated after finishing the focused patterning and the clear focused patterns remained on the non-conducting substrates. Both of droplets and charged particles were generated simultaneously by electrospray of nanoparticle colloid and they were exploited for the focused pattern on non-conducting substrates. Also, charged metal particles generated via spark discharge and droplets for conductive liquid film via electrospray were utilized for metal nanoparticles patterning on the non-conducting substrates.

3.2.2. Prerequisites for focused patterning of charged particles on a non-conducting substrate

Three critical factors were prepared to form a temporary conducting path on the substrates, as shown in Fig. 3.4. First, the droplets were generated by electro spray system which has been well known to produce monodispersed droplets. Second, the critical factor to form conducting path using the liquid is the formation of uniform conducting liquid film on non-conducting substrates. Hydrophilic characteristic of the surface of the substrates is needed to form a uniform film made of the droplets. The hydrophilicity of the surface was modified by a surfactant, which helped forming the uniform liquid film on the surface. Finally, nanoparticle focusing mask was used to form electrostatic lens to guide the particles via ion accumulation on the mask, which is placed on the substrate after surfactant treatment. The mask was originally developed to eliminate the complex process such as the pre-patterning of photoresist (PR) and PR removal after patterning in IAAL method (You et al. 2010).

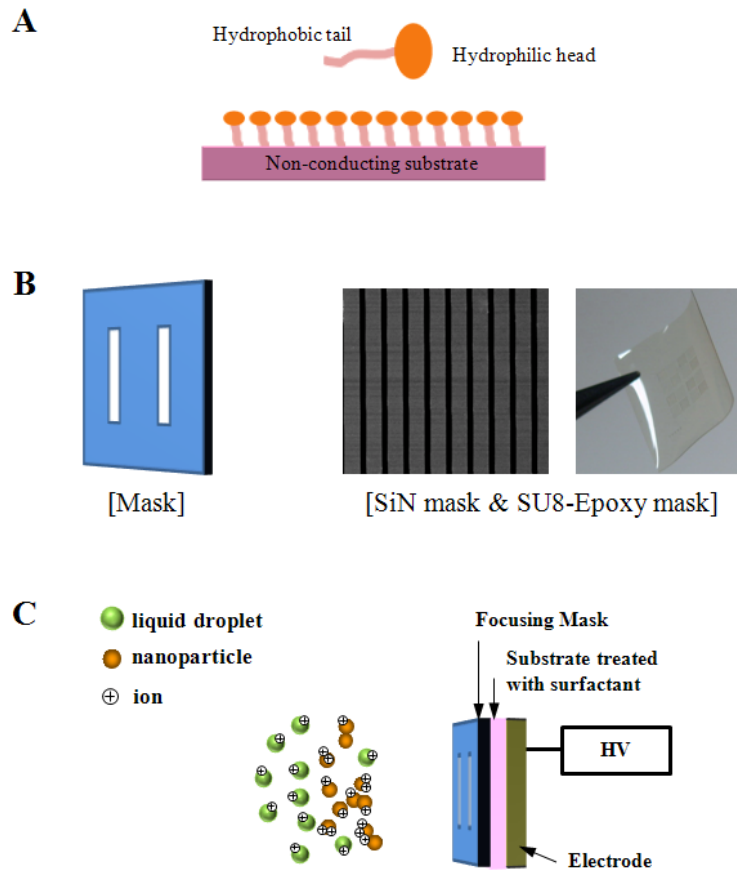


Figure 3.4. Three critical factors for patterning on a non-conducting substrate via the IAAL. (A) Surfactant modifying hydrophilicity of the surface of the substrate. (B) Nanoparticle focusing mask substituting PR pre-patterns and forming electrostatic focusing lens by ion accumulation for the IAAL. (C) Charged particles and droplets supplied via electro spray during deposition.

3.3. Experimental setup

The experimental setup for patterning on a non-conducting substrate consists of electro spray chamber, deposition chamber, syringe pump and high power supply, as shown on Fig. 3.5. Also, we prepared a surfactant, a nanoparticle focusing mask and a electro spray system for droplet generation. First, a non-conducting substrate was treated with the surfactant. The substrate was positioned on an electrode within the deposition chamber and then nanoparticle focusing mask was placed on the surfactant-treated substrate. Positive potential for electro spray and negative potential for deposition of positively charged particles were applied to stainless needle and the electrodes on which the substrate was placed, respectively, as shown in Fig. 3.5.

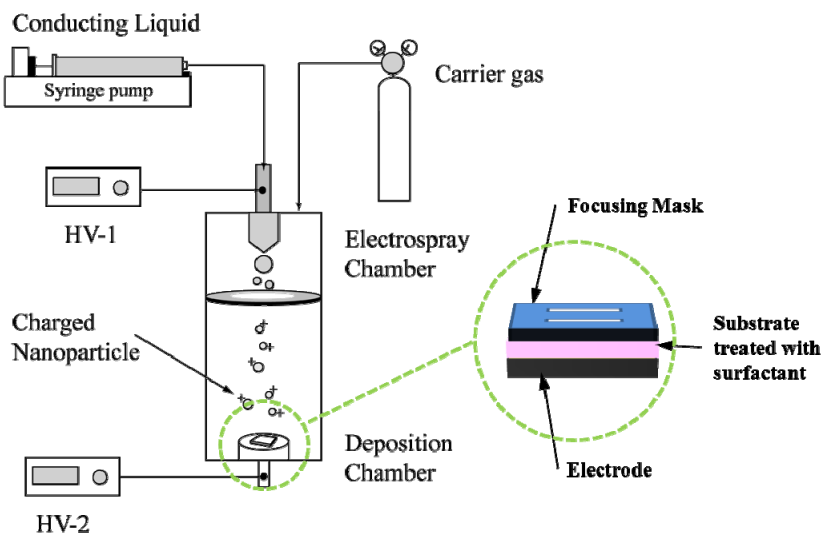


Figure 3.5. Schematic of experimental setup for the patterning

3.3.1. Surface active agent (Surfactant)

Nonylphenoethoxylates($C_9H_{19}-(C_6H_4)-(O-C_2H_4)_n-OH$, Sigma Aldrich) was used as a surfactant to change hydrophilicity of the surface of a non-conducting substrate, which was widely used as a non-ionic surfactant containing one hydrophobic nonylphenol and one hydrophilic ethoxy chain as shown in Fig. 3.6. The surfactant played important role in forming the thin conducting liquid film on the non-conducting substrate with eletrospraying conducting liquid during deposition. The film neutralizes the charged particles deposited on the substrate through a wire connected to electrode shown in Fig. 3.3.

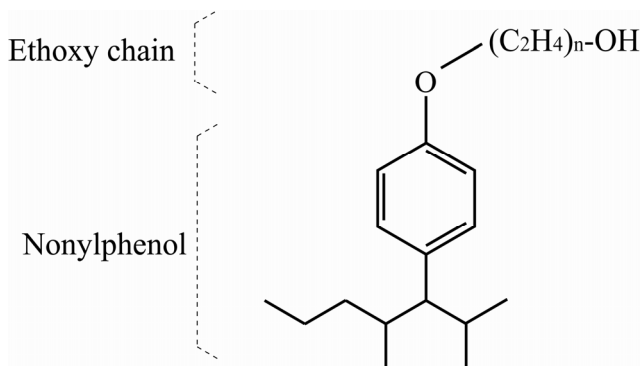


Figure 3.6. Surfactant. (Nonylphenoethoxylates)

3.3.2. Ion-induced Nanoparticle Focusing Mask

Nanoparticle focusing mask was presented to reduce the prepatterning process of photoresist before IAAL deposition, which enabled parallel and high resolution patterning of nanoparticles at low cost (You et al. 2010). The mask is an essential factor in patterning in the non-conducting substrate which is placed on the surfactant treated substrates. In this experiment, silicon nitride masks and an epoxy masks were used to form electrostatic lens by ion accumulation. The mask with 1 μm thick silicon nitride film was prepared for sub-micro scale pattern, which consisted of the opening patterns having 2 μm wide lines and 2 $\mu\text{m} \times 2 \mu\text{m}$ square patterns with 2 μm pitch. The 50 μm thick epoxy mask for several micro patterning had 50 μm wide line and 50 $\mu\text{m} \times 50 \mu\text{m}$ square opening patterns with 50 μm pitch. Fabrication method of the silicon nitride focusing mask was very similar to ways presented by (You et al. 2010) but reactive ion etch process was eliminated to reduce the process cost and fabrication time, as shown in Fig. 3.7. The epoxy masks were prepared by the same process as the case of You et al. 2010.

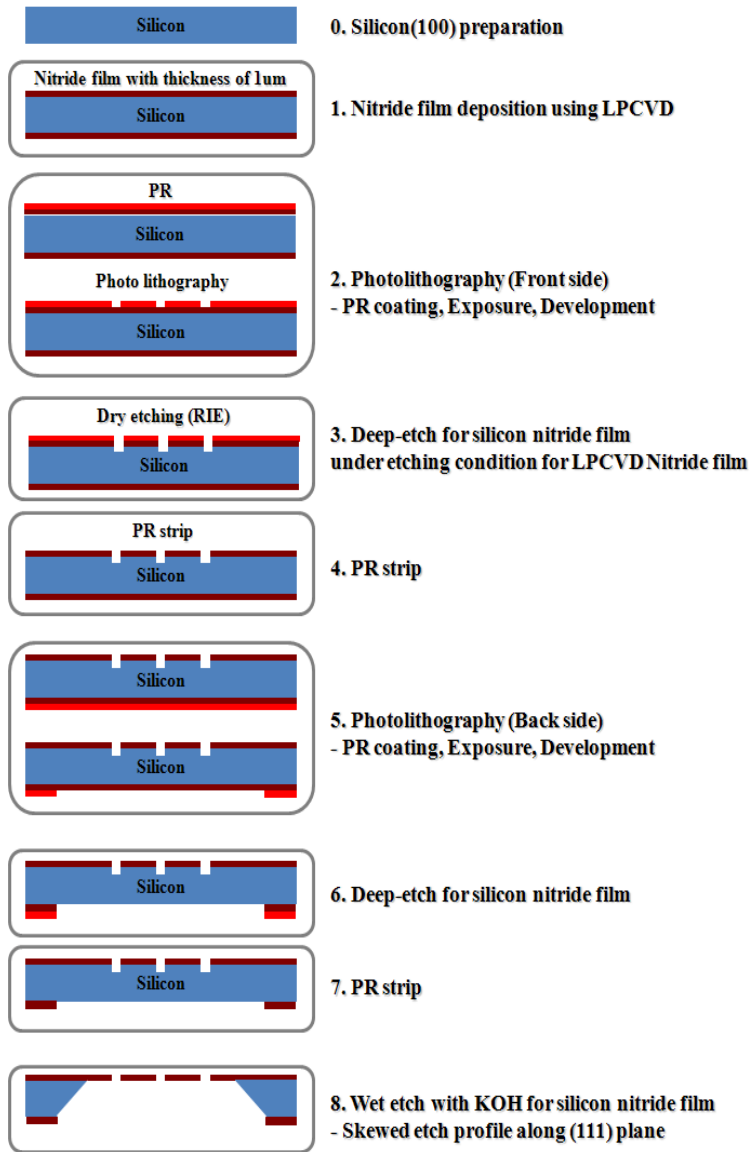


Figure 3.7. Fabrication procedure for silicon nitride mask used in the experiment.

3.3.3. Preparation of liquid droplet and charged particles

Electrospray shown in Fig. 3.8 is a liquid atomization method using electrostatic force to generate charged particles from conducting colloids, which has been widely studied and exploited for nanotechnology (Jaworek and Sobczyk 2008; Park et al. 2010). Droplet size could be expected through the scale law presented by some researches (Delamora and Loscertales 1994; Lenggoro et al. 2000; Lenggoro et al. 2002). The sizes of injected droplets were known to have approximately monodisperse size distribution as long as flow rate to a needle of electro spray system is not too high compared to minimum flow rate for stable cone-jet mode in electrospray system (Hartman et al. 2000; Noymer and Garel 2000).

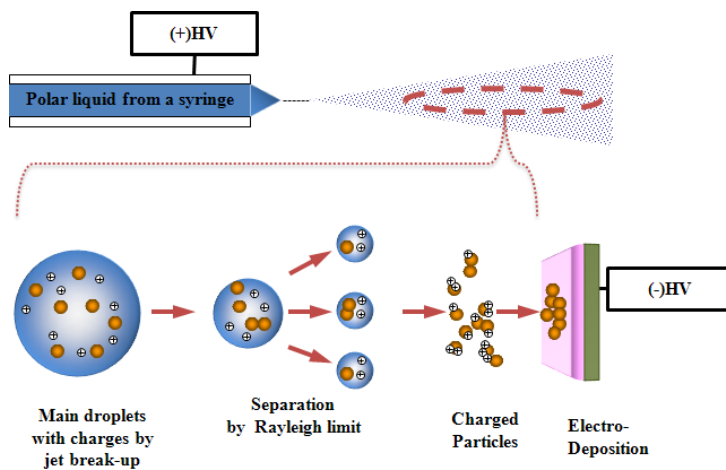


Figure 3.8. Schematic of charged particle deposition via electrospray of conducting liquid on a substrate.

PSL colloid was used to generate charged particles and droplets by electrospray. Two kinds of PSL colloid having different mean diameter of PSL particle were prepared, which one has particles with mean diameter of 30 nm (3030A, Thermo Scientific), and the other has particles with mean diameter of 100 nm (5010A, Thermo Scientific) dispersed in aqueous suspension. PSL particles of 100nm was 60 times diluted volumetrically with ethanol for micro-sized patterns, and 30nm PSL colloidal solution was prepared by mixing 5 times volumetrically with water for nano-sized patterns. In our experiment, needle and liquid flow rate are different with respect to colloid suspension in order to obtain stable cone-jet mode at lowest flow rate in Table 3.1. Colloid solution of 30nm PSL particles and 100nm PSL particles were supplied with flow rate of 50 $\mu\text{l/h}$ and 150 $\mu\text{l/h}$ from the syringe pump, respectively. The voltage of 5.1 kV was applied to electrospray needle with N_2 gas of flow rate of 2 liter / min (lpm) for 100 nm PSL solution while the voltage of 9.1kV was applied for 30 nm PSL colloidal solution with CO_2 gas of flow rate of 1.5 lpm to prevent electrical discharge near the sharp electrospray needle at that high voltage.

Table 3.1. Electrospray condition with respect to liquids.

Liquid	Outer diameter of a needle	Inner diameter of a needle	Maximum flow rate of liquid	Minimum flow rate of liquid
Water	510 μm	260 μm	50 $\mu\text{l/h}$	40 $\mu\text{l/h}$
Ethanol	810 μm	510 μm	200 $\mu\text{l/h}$	100 $\mu\text{l/h}$

The size of injected initial droplet could be calculated using the scaling law presented in [Equation 3.1] with the condition that dielectric constant of polar liquid exceeds 6 and electrical conductivity is larger than 1E-5 S/m (de Juan and de la Mora 1997; Lenggoro et al. 2002).

$$D_d = G(\varepsilon, \mu) \times \left(\frac{Q\varepsilon\varepsilon_0}{K} \right)^{1/3} \quad \text{[Equation 3.1]}$$

Where D_d is diameter of the droplet size in cm, and Q is flow rate of liquid from syringe pump in cc/sec, and K is electrical conductivity of liquid in S/m. The value of G was chosen to be 0.6 for water and ethanol from data of the previous research (Lenggoro et al. 2000). The size of initial droplet in this experiment was expected through the scaling law as shown in Table 3.2. Smaller water droplets having 30nm PSL were thought to be advantageous to nano-scaled patterning.

Table 3.2. Droplet size calculated from scaling law.

Liquid	Conductivity (S/m)	G	ε	Q (cc/sec)	D_d (nm)
Ethanol	3.00E-05	0.6	24	4.2E-05	4011.336
Water	2.00E-04	0.6	81	1.4E-05	2207.523

3.4. Results and discussion

3.4.1. Formation of conducting liquid film

Formation of liquid thin film was checked with silver pads which were separated with gap of about 2mm and formed on a PET film, as shown in Fig. 3.9. Surfactant-treated PET film with the pads was placed on the electrode in the deposition chamber. Ethanol with flow rate of 150 $\mu\text{L/h}$ was injected to the pad via electrospray and the pads were connected to multi-meter to check whether the conducting layer was formed. Voltage of 3.8 kV and -1 kV were applied to electrospray needle and the substrate, respectively. Resistance of several mega ohm was measured during electrospraying of ethanol, which means the pads on the PET film were electrically connected each other via the thin liquid film formed by the droplets. Current flowing through the temporary conducting liquid film was measured with the experiment setup shown in Fig. 3.10A. The experiment was done with a bare electrode, the electrode covered with PET film without surfactant treatment, and the electrode covered with a surfactant-treated PET film. Condition of electrospray was fixed during the experiment. Interestingly, current of about 0.8 nA was measured through a surfactant-treated PET film in comparison with the case of the electrode covered with PET film without surfactant treatment even though the value of the current is lower than the case of bare electrode, as shown in Fig. 3.10B. These results show that droplets via electrospray could form the temporary conducting film on the non-conducting substrates and supply the way to neutralize the charged particles.

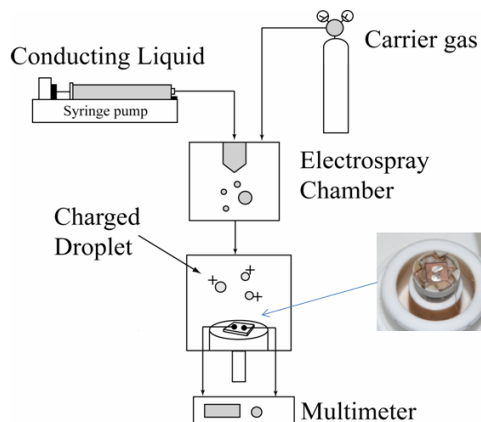


Figure 3.9. Schematic of experimental setup for checking connectivity.

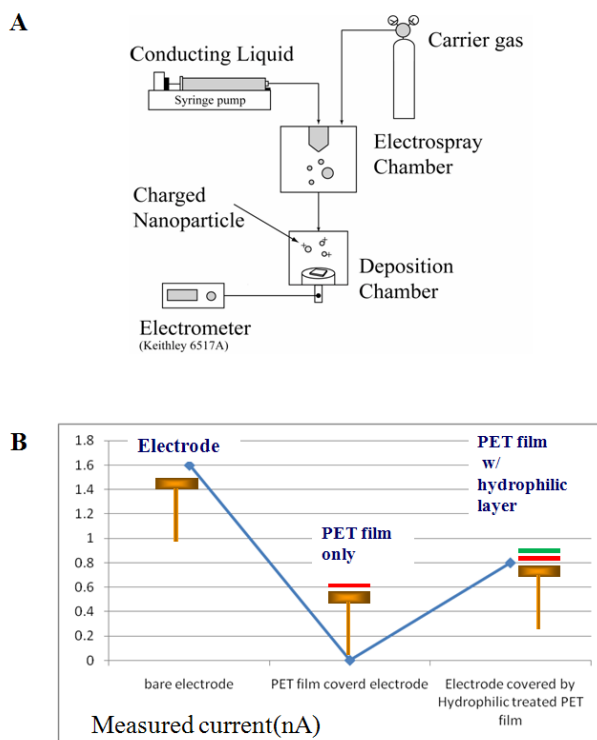


Figure 3.10. Current measurement through the temporary conducting film. (A) Schematic of experimental setup. (B) Current measured with respect to surface treatment of the substrate.

3.4.2. Focused patterning on a non-conducting substrate

Focused patterns were obtained with the method as mentioned before. Voltage of 9.1kV and -0.8kV were applied to electro spray needle and the substrate, respectively, for electro spraying 30 nm PSL colloidal solution with CO₂ of flow rate of 1.5 lpm. The deposition time was 30 min. Line patterns with width of 420 nm (Fig. 3.11C) deposited on 0.7 mm thick glass substrate (Fig. 3.11A) with the silicon nitride mask (Fig. 3.11B) having 2 μ m wide line openings.

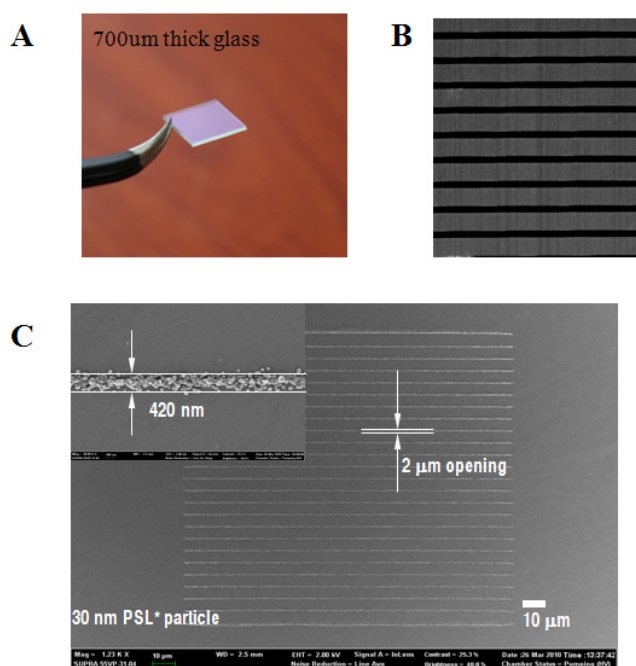


Figure 3.11. Patterns of PSL particles on the thick glass. (A) Optical image of 0.7 mm thick glass substrate. (B) SEM image of the silicon nitride mask having line type openings (C) 420 nm line patterns consisting of 30 nm-sized PSL particles. (Adopted from You et al. 2010)

Also, the patterning method could be applicable to flexible PET film. The voltage of 5.1 kV and -0.4 kV were applied to electro spray needle and the substrate, respectively. N₂ gas was fed to deposition chamber with flow rate of 2 lpm and the deposition time was 15 min. Figure 3.12C shows approximately 10 μm wide line and 12 μm x 12 μm square patterns of 100 nm PSL particles on the PET film (Fig. 3.12A) via the epoxy mask (Fig. 3.12B) having 50 μm line and 50 μm x 50 μm square openings.

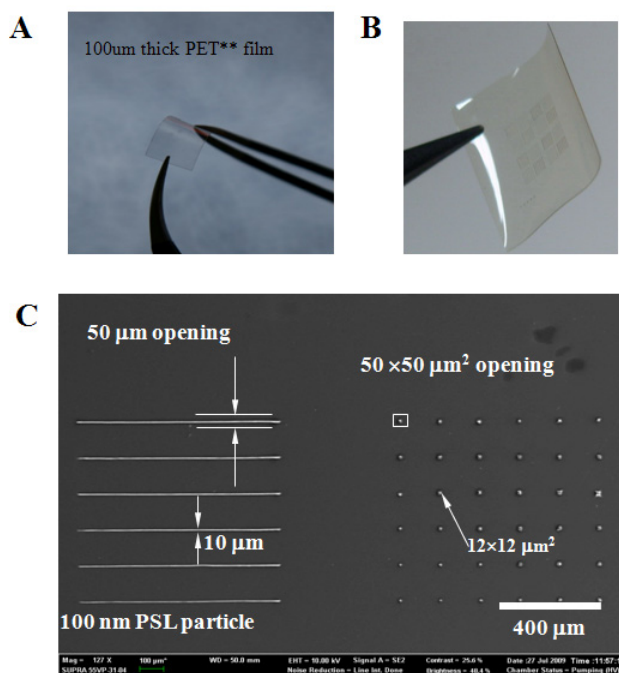


Figure 3.12. Patterns of PSL particles on the flexible PET film. (A) Optical image of 0.1 mm flexible PET film. (B) Photography of the epoxy mask (C) 10 μm line patterns and 12 x 12 μm^2 consisting of 100 nm-sized PSL particles. (Adopted from You et al. 2010)

This method based on IAAL can be utilized to pattern conducting line by electro spraying the metal nanoparticles used in inkjet patterning method. Conducting micro wires with silver nanoinks (InkTek, PR-030) were patterned with higher resolution in compared to normal inkjet technology. Figure 3.13 shows patterning of a micro conducting wire with silver ink on the Kapton film. We removed the ground ring from the deposition chamber, and chamber wall was used as ground electrode for electro spray to reduce the deposition of charged silver nanoink, as shown in Fig. 3.13A. Nanoink colloid was prepared by mixing 5 times volumetrically with ethanol for obtaining stable cone-jet because the nanoink was dispersed in organic solvent and it was difficult to electro spray the original nanoinks without addition of ethanol. The nanoink was supplied to the needle for electro spray with flow rate of 100 $\mu\text{l/h}$ and voltage of 3.8 kV and -0.3 kV were applied to electro spray needle and the substrate, respectively. CO_2 was fed to deposition chamber with flow rate of 1.5 lpm and the deposition time was 30 min. Figure 3.13B and 3.13C show the SEM images of the wire and the measured current versus voltage (I-V) curve which exhibits an ohmic behavior. Conducting Ag microwire with 8 μm width was made on Kapton film by the convergent deposition of silver nanoink under the epoxy focusing mask having a 100 μm wide line opening. The resistivity of 5.8 $\mu\Omega\text{cm}$ was obtained by measuring the resistance of 3.3 ohm and the cross section of 17.6 μm^2 by a probe station and AFM, respectively, which was about four times as high as that of bulk silver.

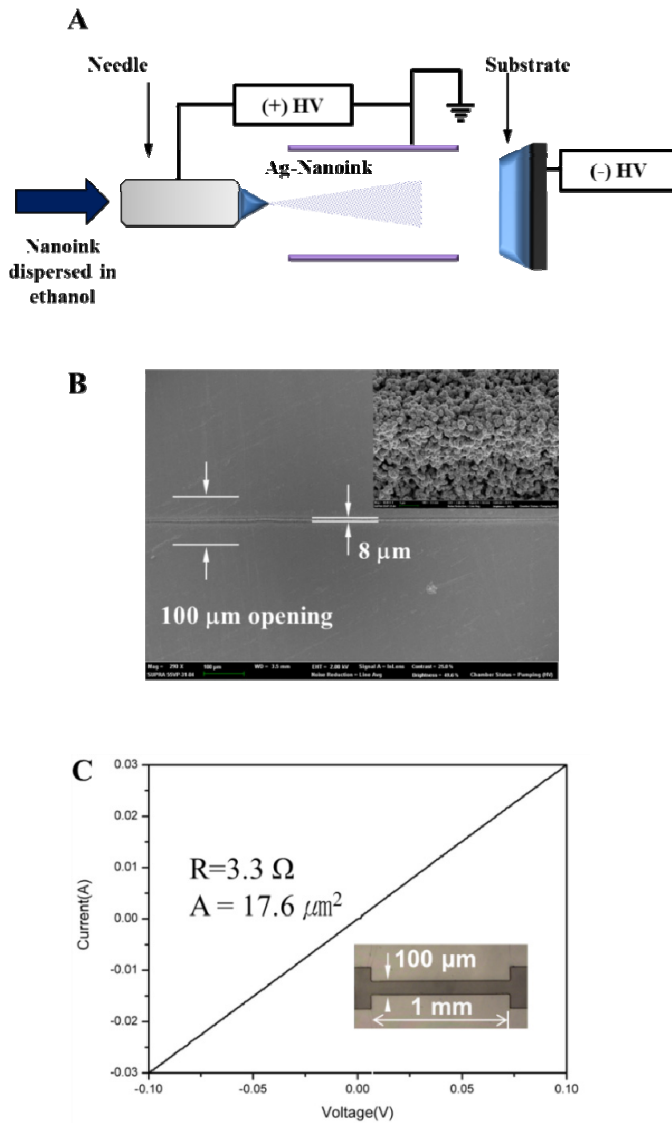


Figure 3.13. Patterning of a micro conducting wire with silver ink on the Kapton film. (A) Schematic of experimental setup. (B) SEM image of the 8 μm wide conducting wire. (C) Voltage and current relation for the conducting wire and inset shows the epoxy mask used for patterning. (Adopted from Lee 2010)

Charged gold particles generated via spark discharge were patterned on the PET film. Spark generated gold particles and droplets via electrospray were prepared independently shown in Fig. 3.14A. The droplets played the role in forming the conducting thin film and then the charged nanoparticles were deposited on the PET film. Water was supplied to the needle for electrospray with flow rate of 50 $\mu\text{l/h}$ and voltage of 4.7 kV and -4 kV were applied to electrospray needle and the substrate, respectively. CO_2 and N_2 were fed to deposition chamber with flow rate of 1.5 lpm and to spark chamber with flow rate of 2 lpm, respectively. The deposition was lasted for 120 min. Figure 3.14B and 3.14C show the SEM image of the 270 nm line patterns and 350 x 350 nm^2 square patterns, respectively. Therefore, separately generated charged nanoparticles and droplets could be patterned on the non-conducting substrates with this method.

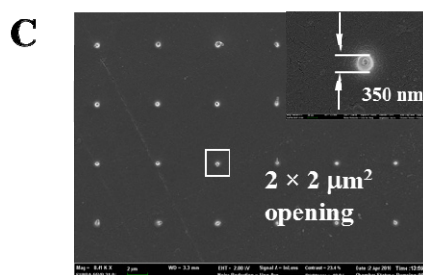
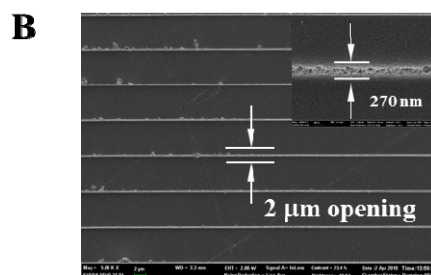
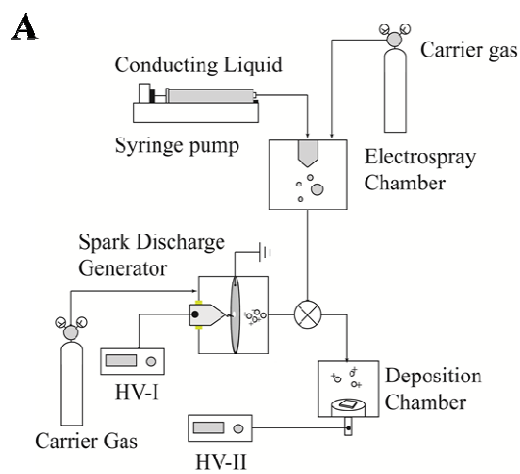


Figure 3.14. Patterning of gold nanoparticles generated via spark discharge generator on the PET film. (A) Schematic of experimental setup. (B) SEM image of the 270 nm line patterns. (C) 350 x 350 nm² square patterns.

3.5. Conclusion

We proposed the method for focused patterning of charged particles on a non-conducting substrate. The temporary path to neutralize the particles was devised to eliminate the charges from incoming charged particles. The formation of conductive liquid film on the substrate was based on hydrophilic characteristic of the surface. We used a surfactant to change the hydrophobic into hydrophilic surface and prepared droplets of conducting liquid via electrospray for formation of the liquid film. Nano and micro scaled focused patterns was obtained with PSL particles via this method, and also the micro conducting wires with silver nanoinks were easily patterned with higher resolution in compared to normal inkjet technology. Sub-micro scaled gold nanoparticle patterns also were realized with charged particles via spark discharge generator. Charged nanoparticle patterns on thick non-conducting substrates can be utilized for applications such as displays, flexible solar cell and electronics.

3.6. References

- Barry, C. R., Gu, J. and Jacobs, H. O. (2005). Charging Process and Coulomb-Force-Directed Printing of Nanoparticles with Sub-100-nm Lateral Resolution. *Nano Letters*, 5, 2078-2084.
- de Juan, L. and de la Mora, J. F. (1997). Charge and Size Distributions of Electro spray Drops. *Journal of Colloid and Interface Science*, 186, 280-293.
- Grace, J. and Marijnissen, J. (1994). A review of liquid atomization by electrical means. *Journal of Aerosol Science*, 25, 1005-1019.
- Hartman, R. P. A., Brunner, D. J., Camelot, D. M. A., Marijnissen, J. C. M. and Scarlett, B. (2000). Jet break-up in electrohydrodynamic atomization in the cone-jet mode. *Journal of Aerosol Science*, 31, 65-95.
- Jacobs, H. O. and Whitesides, G. M. (2001). Submicrometer Patterning of Charge in Thin-Film Electrets. *Science*, 291, 1763-1766.
- Lastow, O. and Balachandran, W. (2007). Novel low voltage EHD spray nozzle for atomization of water in the cone jet mode. *Journal of Electrostatics*, 65, 490-499.
- Lee, J. (2010). Study on the conducting microline patterning on a flexible non-conducting substrate using nanoparticle focusing mask, Master thesis in Seoul National University.
- Lenggoro, I. W., Okuyama, K., de la Mora, J. F. and Tohge, N. (2000). Preparation of ZnS nanoparticles by electro spray pyrolysis. *Journal of Aerosol Science*, 31, 121-136.
- Lenggoro, I. W., Xia, B., Okuyama, K. and de la Mora, J. F. (2002). Sizing of

- colloidal nanoparticles by electrospray and differential mobility analyzer methods. *Langmuir*, 18, 4584-4591.
- Noymer, P. D. and Garel, M. (2000). Stability and atomization characteristics of electrohydrodynamic jets in the cone-jet and multi-jet modes. *Journal of Aerosol Science*, 31, 1165-1172.
- Park, J.-U., Lee, S., Unarunotai, S., Sun, Y., Dunham, S., Song, T., Ferreira, P. M., Alleyne, A. G., Paik, U. and Rogers, J. A. (2010). Nanoscale, Electrified Liquid Jets for High-Resolution Printing of Charge. *Nano Letters*, 10, 584-591.
- Seemann, L., Stemmer, A. and Naujoks, N. (2007). Local Surface Charges Direct the Deposition of Carbon Nanotubes and Fullerenes into Nanoscale Patterns. *Nano Letters*, 7, 3007-3012.
- You, S., Han, K., Kim, H., Lee, H., Woo, C. G., Jeong, C., Nam, W. and Choi, M. (2010). Nanoparticle patterning: High-Resolution, Parallel Patterning of Nanoparticles via an Ion-Induced Focusing Mask. *Small*, 6, 2146-2152

This page is intended to be blank

Chapter 4.

Enhancement of Luminescence of OLED using Gold Nanoparticles

4.1. Introduction

Organic Light Emitting Diode (OLED) exploiting electroluminescence from organic materials have been widely studied due to the realization of full color display with low energy consumption and its low-cost fabrication since multi-layer OLED was reported by (Tang and VanSlyke, 1987). Efficiency of OLED has been improved using multi-layer structure, cathode with low work function material (Tang et al. 1989) and buffer layer between anode and organic materials (Deng et al. 1999).

Recently, noble metal nanoparticles have been used to increase efficient of OLED with the principle of localized surface plasmon resonance, LSPR. (Fujiki et al. 2010; Tanaka et al. 2011) Gold nanoparticles (Fujiki et al. 2010) and gold nanorods (Tanaka et al. 2011) deposited on anode of OLED were utilized to enhance the emission efficiency of OLED with the LSPR of gold nanostructures. Another interesting feature of gold nanoparticles is charge trapping characteristics (Li et al. 2008) which was used for non-volatile memory application. (Lee 2010) For gold nanoparticles smaller than 10 nm, absorption is more dominant than scattering so those particles in the electroluminescence devices could affect electrical characteristics of the devices instead of enhancement of optical properties by LSPR. The distance of metal nanoparticles from emitting layer of OLED is a critical parameter to maximize its luminescence efficiency utilizing these features of the gold nanostructure. However, positioning nanoparticles in the middle of the OLED could be limited because wet-processed metal nanoparticles are

difficult to be deposited on organic materials without contamination or damage to them. Aerosol based nanoparticles could be applicable to any position in the OLED devices without any stabilizer or surfactant, and especially the spark discharge generator could be used controlling their sizes and number concentration with a facile way as well as easily positioning them at desired positions in the organic materials.

We fabricated organic light emitting diode using gold nanoparticles generated via pin-to-plate type spark discharge and demonstrated the increase of external quantum efficiency (EQE) of OLED positioning gold nanoparticles at a desired position in the middle of organic materials of OLED (Sung, H et al 2012). Interestingly, gold nanoparticles less than 10nm were thought to be effective to balance the charge carrier such as holes and electrons injected into emitting layer of OLED instead of enhancement of scattering by the particles. Effect of sizes of gold nanoparticles on EQE was examined by changing the parameters in spark discharge in order to investigate whether balancing of charge carriers or scattering by the particles is more dominant.

4.2. Background and Experimental Procedure

4.2.1. Fluorescence of organic material

Fluorescence is a luminescence phenomenon for emission of light via radiative relaxation from a molecule called ‘fluorophore’ in an electronically excited state (Fort and Grésillon 2008). Luminescence from molecules excited by specific photons is called photoluminescence which could be divided into fluorescence and phosphorescence. They have been explained with respect to electronic configuration and emission pathways shown in Fig. 4.1. Fluorescence is a phenomenon that lights are emitted via transition from a singlet state of molecule to ground state while phosphorescence is based on transition from a triplet state. For fluorescence, a material absorbs light at a specific wavelength and subsequently emits light of longer wavelength than the absorbing wavelength after fluorescence lifetime of 10^{-9} seconds.

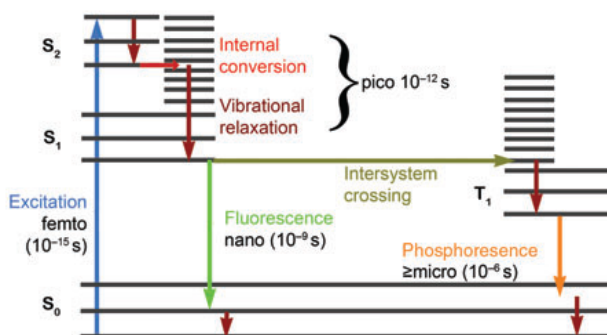


Figure 4.1. The Jablonski diagram displaying the energy states of a molecule. (Adopted from Lichtman and Conchello 2005)

Quantum efficiency (Q) is usually defined as the ratio of radiative relaxation to total relaxation including radiative and non-radiative relaxation in the absence of other absorbing medium in [Equation 4.1] (Fort and Grésillon 2008).

$$Q = \frac{\Gamma_{rad}}{\Gamma_{rad} + \Gamma_{nonrad}} \quad \text{[Equation 4.1]}$$

where Γ_{rad} and Γ_{nonrad} are radiative decay rate and non-radiative decay rate, respectively. The quantum efficiency could be changed dramatically by introducing metals such as nanoparticles or thin film near the organic material showing fluorescence, fluorophore, (Geddes and Lakowicz 2002) and modified adding the effects by metals in [Equation 4.2]

$$Q_{metal} = \frac{\Gamma_{rad} + \Gamma_{metal}}{\Gamma_{rad} + \Gamma_{metal} + \Gamma_{nonrad}} \quad \text{[Equation 4.2]}$$

where Q_{metal} is represented quantum efficiency with metal nanoparticle or film. Localized surface plasmon resonance of metal nanoparticle can increase radiative decay (Γ_{metal}) with the introduction of metal and the corresponding quantum efficiency increases. In contrast, quenching by metal nanoparticles near the fluorophores increases non-radiative decay and the resultant efficiency decreases. These principles should be considered to improve the quantum efficiency of OLED with metal nanoparticles generated via the spark discharge generator.

4.2.2. OLED fabrication with gold nanoparticles

We fabricated an OLED having the layers of ITO/NPB/Alq3/LiF/Al shown in Fig. 4.2A and placed gold nanoparticles produced by the pin-to-plate type SDG at the optimum position where was the distance of 20nm from the interface of N,N'-Di-[(1-naphthalenyl)-N,N'-diphenyl]-(1,1'-biphenyl)-4,4'-diamine (NPB) and tris(8-hydroxyquinoline)aluminum (Alq3) layer in the middle of the NPB layer of the OLED. (Sung, H et al 2012) NPB and Alq3 shown in Fig. 4.2B-C were used as a hole-transfer layer and an electron transfer layer, respectively. The latter was also used as an emitting layer with fluorescence peak of about 520nm. Figure 4.3A shows an energy band diagram for the fabricated OLED consisting of organic bilayer.

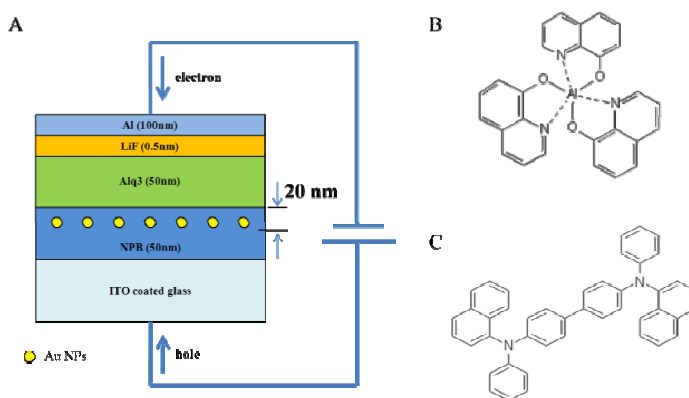


Figure 4.2. The Organic Light Emitting Diode fabricated in the experiment. (A) The schematic of the OLED configuration. (B) Molecular structure of Alq3 used as both emitting layer and electron transfer layer. (C) Molecular structure of NPB.

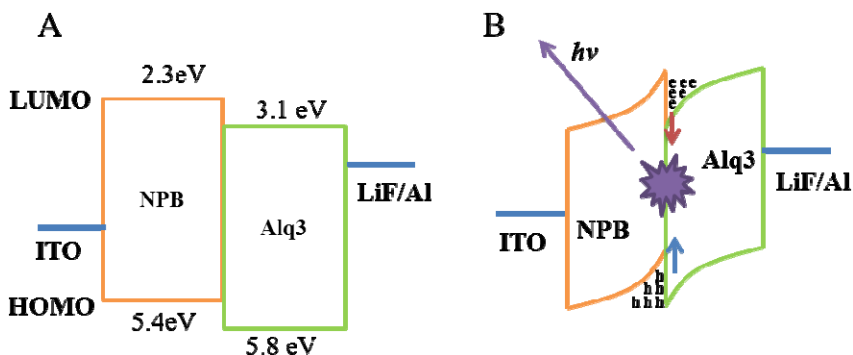


Figure 4.3. Energy band diagram for the organic bilayer of OLED fabricated in the experiment. (A) Energy band of the OLED without electrical potential. (B) Energy band bending of the OLED with electrical potential and the resultant recombination.

Recombination of electrons injected from a cathode and holes from an anode, and the resultant emission shown in Fig. 4.3B were known to occur in Alq3 near the interface to a distance of about 30nm when electric potential was applied to each electrode. (Tang and VanSlyke, 1987).

An ITO coated glass substrate was cleaned to remove organic contamination before organic film deposition. The glass was sonicated with detergent for 15 minutes and rinsed with DI water and then sequentially sonicated with acetone and isopropyl alcohol (IPA) for 15 minutes, respectively. Finally, the glass substrate was treated with UV ozone to reduce the carrier injection barrier of ITO before entering a vacuum evaporator. 50 nm-thick NPB film and 50 nm-thick Alq3 film were sequentially deposited on the cleaned ITO coated glass with deposition rate

of 1 Å/sec, and 5 Å-thick LiF film and 100 nm-thick Al film as a cathode electrode were deposited with deposition rate of 0.2 Å/sec and 1 Å/sec, respectively. The deposition in the vacuum evaporator was done at the pressure of 0.5×10^{-7} Torr. All processes except glass cleaning process were carried out in the globe box filled with N₂ or vacuum environment to prevent degradation of the organic material by oxygen and humidity and so on. Gold nanoparticles were generated via the pin-to-plate type SDG in the globe box. A pin electrode of diameter of 1mm was made to have a tip and the grounded plate electrode was made to have an exit hole of 1-mm-diameter in the center. The gap between the electrodes kept 1mm during the experiment and breakdown voltage of about 4.4 kV at N₂ atmosphere was measured. The experimental equipment is shown in Fig. 4.4. Initially, applied setting potential from the HV, the charging resistance (R) and the capacitance (C) for the spark discharge generator were set as 5 kV, 20 Mohm and 2nF for gold nanoparticles generation, respectively. Deposition of the particles via the SDG in the middle of NPB layer was done in the deposition chamber for 5 min.

In previous study, we embedded gold nanoparticles with GMD of 6 nm into the OLEDs having different positions in the middle of NPB film and found out the optimum position for enhancing electroluminescence of the OLED (Sung, H et al 2012). The gold nanoparticles were deposited with respect to the distance of 10, 20, 30, 40 and 50 nm from the interface of Alq₃ and NPB layer in the middle of NPB layer.

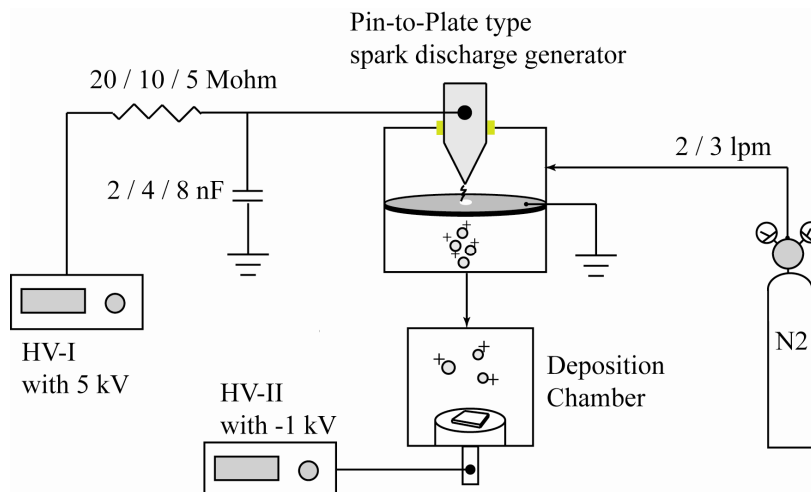


Figure. 4.4. Schematic of experimental equipment for gold nanoparticle deposition in the middle of the NPB film of the OLED.

The distance of 20nm from the interface of Alq₃ and NPB layer was known to be the optimum position for maximizing the external quantum efficiency (EQE) of the OLED. In this experiment, we tried to investigate the effect of the size of gold nanoparticles on the EQE and find out an optimum size of gold nanoparticles at the optimum position. Various sized gold nanoparticles were generated by controlling parameters of spark discharge as shown in Fig. 4.5. We changed sizes of the particles adjusting the capacitance of 2, 4 and 8 nF in the circuit shown in Fig. 4.5A to increase spark energy, and kept the value of RC constant changing the resistance of the resistor of 20, 10 and 5 Mohm in the circuit, respectively, in order to maintain the fixed spark frequency. In addition, the smaller particles than the case of spark discharge with capacitance of 2nF, resistance of 20 Mohm and carrier gas, N₂ with flow rate of 2 lpm were obtained with carrier gas

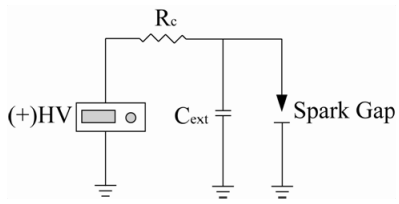
with flow rate of 3 lpm, as shown in Fig. 4.5B. The distribution of gold nanoparticles was examined through SMPS system, SEM and TEM analysis. Characteristic of current density (J), voltage (V) and luminescence (L) were measured with Keithley 2400 source/meter and Newport 818-SL photodetector at room temperature and under ambient condition. EQE is defined as the ratio of the number of photons emitted by the OLED into the viewing direction to the number of electrons injected and was calculated using [Equation 4.3] to [Equation 4.5] (Forrest et al. 2003)

$$\eta_{ext} = \frac{\int \lambda I_{det}(\lambda) d\lambda}{f I_{OLED} \int \lambda \eta_{det}(\lambda) d\lambda} \quad [\text{Equation 4.3}]$$

$$\eta_{det} = \frac{hcR(\lambda)}{q\lambda} \quad [\text{Equation 4.4}]$$

$$R(\lambda) = \frac{I_{det}(\lambda)}{f(\lambda)P_{OLED}(\lambda)} \quad [\text{Equation 4.5}]$$

where I_{det} is the incremental photocurrent generated by photodetector, h is Planck's constant, q is the electronic charge, I_{OLED} is the OLED current, f is the fraction of light emitted to that coupled into the detector, λ is the wavelength and c is the speed of light in vacuum.

A**Spark Energy**

$$E_{spark} = \frac{1}{2} C_{ext} V_{dis}^2$$

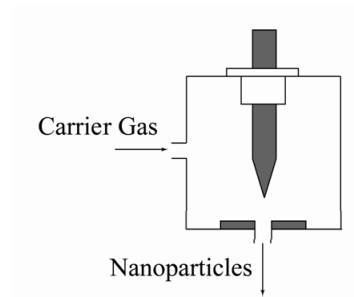
B**Carrier gas flow**

Figure 4.5. Control of the sizes of nanoparticles in spark discharge. (A) Size control by changing capacitance in the circuit. (B) Size control by changing the flow rate of the carrier gas.

4.3. Results and Discussions

4.3.1. The sizes of gold nanoparticles with respect to spark parameters.

Various sizes of gold nanoparticles were prepared to find out optimum sizes of the nanoparticles at the known optimum position of the nanoparticles in the OLED. Their size distribution was measured with the same way as used in Fig. 2.5. Gold nanoparticles via pin-to-plate type spark discharge generator were useful to investigate the effect of sizes of nanoparticles because it generates less agglomerated particles, as shown in Ch. 2. We compared the size distribution of gold nanoparticles with respect to chamber configuration; pin-to-plate type (PPSDG) versus rod-to-rod type configuration (RRSDG). Gold nanoparticles from PPSDG were generated with smaller and narrow size distribution compared to RRSDG, as shown in Fig. 4.6. Both spark discharge generators were operated with the same electrical circuit with capacitance of 2nF and resistance of 20 Mohm with carrier gas with flow rate of 2 lpm and with the gap distance of 1 mm.

For PP-SDG, particles are less agglomerated than for RR-SDG, as shown in Fig. 4.6A. Mobility size distributions based on SMPS measurements also shows the same trends as in Fig. 4.6B. The geometric mean diameter (GMD, d_g) of gold nanoparticles produced via the PP-SDG was found to be much smaller (GMD: 6.0 nm) than that via the RR-SDG (GMD: 9.4 nm). In addition, the PP-SDG generated particles having a narrower size distribution

(geometric standard deviation, σ_g : 1.4) than that of the RR-SDG (σ_g : 1.58). These gold nanoparticles were embedded at the optimum position in the OLED.

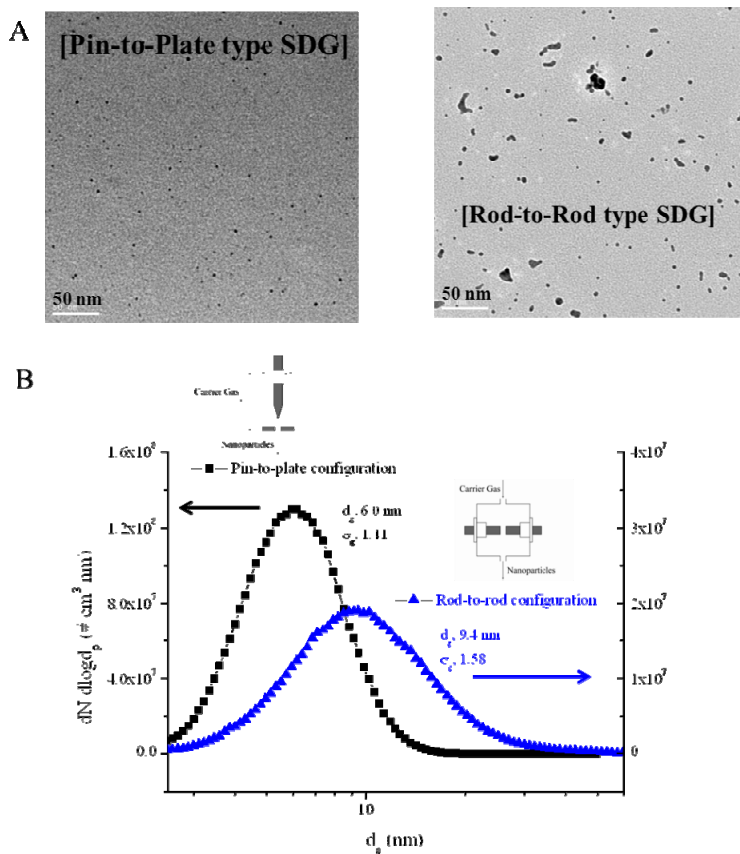


Figure 4.6. Gold nanoparticles generated by spark discharge generators with a gap distance of 1 mm, N₂ gas flow rate of 2 lpm and applied positive potential of 5kV. (A) TEM images of gold nanoparticles for PPSDG and RRS DG. (B) Mobility diameter based size distribution for both configurations.

Various sized gold nanoparticles were generated adjusting the capacitance of 2, 4 and 8 nF while the value of RC was kept fixed to maintain constant spark frequency so the corresponding resistance was set 20, 10 and 5 Mohm, respectively. Mobility based diameters were obtained by SMPS analysis as shown in Fig. 4.7. Figure 4.8 shows TEM images for gold nanoparticles and SEM images for gold nanoparticles deposited on the ITO glass with respect to each capacitance. The sizes of gold nanoparticles and aggregates increase as capacitance in the spark discharge increases because larger capacitance means higher spark energy. From the SEM images, number density of the particles was found to be about one particle per $33 \times 33 \text{ nm}^2$.

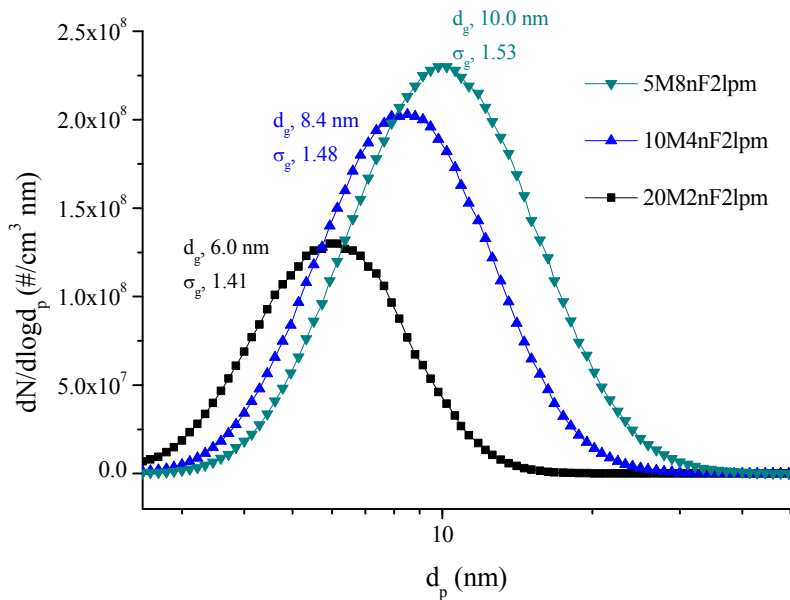


Figure 4.7. Mobility diameter based size distribution with respect to the capacitance in the electrical circuit.

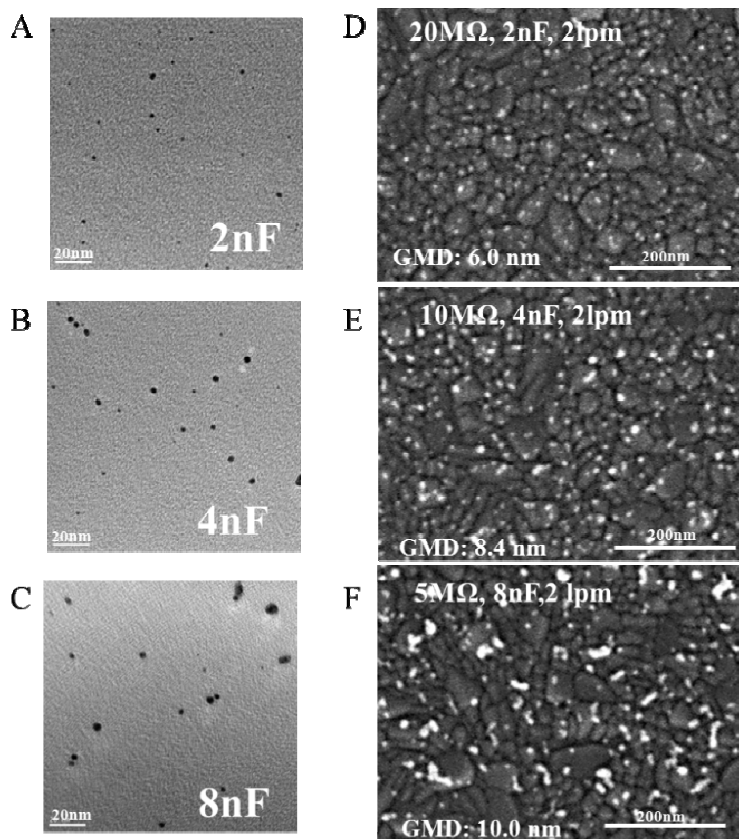


Figure 4.8. Gold nanoparticles generated adjusting the capacitances of the external capacitor. (A,D) TEM and SEM images of gold nanoparticles via the SDG with nitrogen flow rate of 2 lpm, resistance of 20 Mohm and capacitance of 2 nF. (B,E) TEM and SEM images of gold nanoparticles via the SDG with resistance of 10 Mohm and capacitance of 4 nF. (C,F) TEM and SEM images of gold nanoparticles via the SDG with resistance of 5 Mohm and capacitance of 8 nF.

In addition, smallest particles with GMD of 5.5nm and GSD of 1.41 were obtained via spark discharge with capacitance of 2nF and resistance of 20 Mohm and carrier gas with the flow rate of 3 lpm as shown in Fig. 4.9. From the SEM images, number density of the particles was found to be about one particle per 25 x 25 nm².

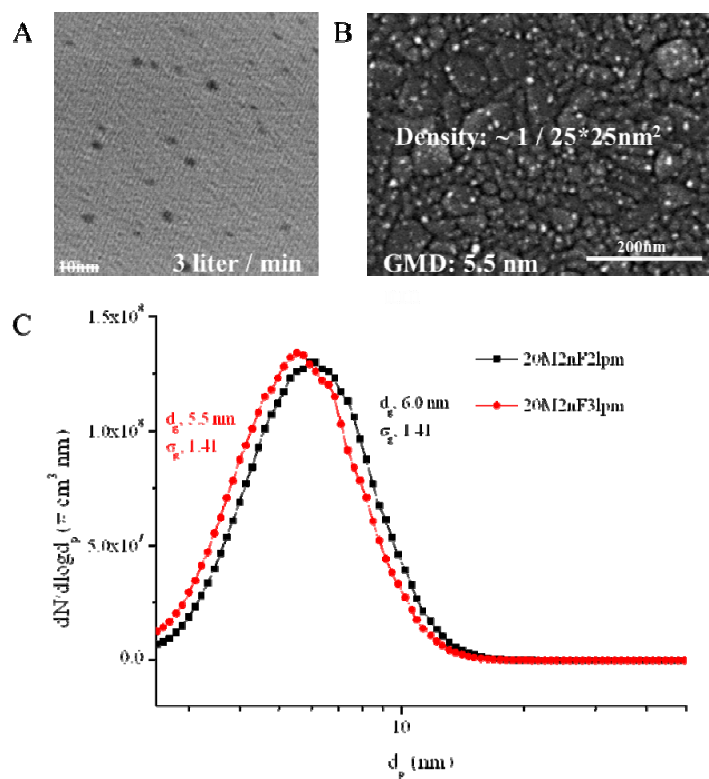


Figure 4.9. Gold nanoparticles generated adjusting the flow rate of carrier gas. (A) A TEM image (B) A SEM image (C) Mobility based size distribution of gold nanoparticles via the SDG with resistance of 20 Mohm and capacitance of 2 nF depending on nitrogen flow rate.

4.3.2. Characteristics of OLED with respect to the sizes of gold nanoparticles.

Optimum size of the nanoparticles was found out at known optimum distance of 20 nm from the interface of Alq3 and NPB. First, OLEDs were fabricated with various sized gold nanoparticles adjusting the capacitance of 2, 4 and 8 nF, respectively. Characteristics of current density versus driving voltage for each cases show the change of current density as sizes of particles and aggregates increase, as shown in Fig. 4.10A. Current density increased at voltage beyond 3V, and external quantum efficiency (EQE) of the OLED increased as sizes of gold nanoparticles decreased, as shown in Fig. 4.10A and B. Second, flow rate of carrier gas was increased to obtain the smaller sized particles than the case with capacitance of 2nF. An OLED was fabricated with those particles and its characteristic was compared with an OLED with larger particles. In this case, external quantum efficiency increased while current density decreased as sizes of gold nanoparticles decreased, as shown in Fig. 4.11A and B. External quantum efficiency (EQE) of the OLED with smallest gold nanoparticle in the experiment increased up to maximum of 44 % in comparison with OLED without gold nanoparticles, as shown in Fig. 4.10B and 4.11B. The enhancement in EQE of the OLED with optimum sized gold nanoparticles at the optimum position was about twice as high as that of recent research with Alq3 used as emitting layer (Y. Xiao 2012).

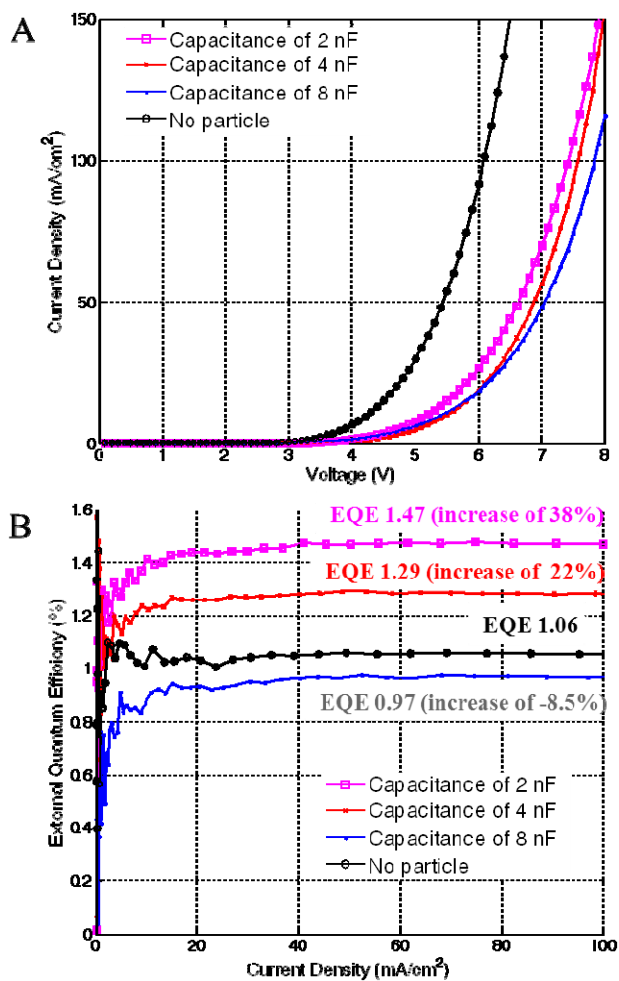


Figure 4.10. Characteristics of the OLED devices with respect to capacitance in the electric circuit (A) Characteristics of current density versus voltage driving the device. (B) External quantum efficiency of the devices.

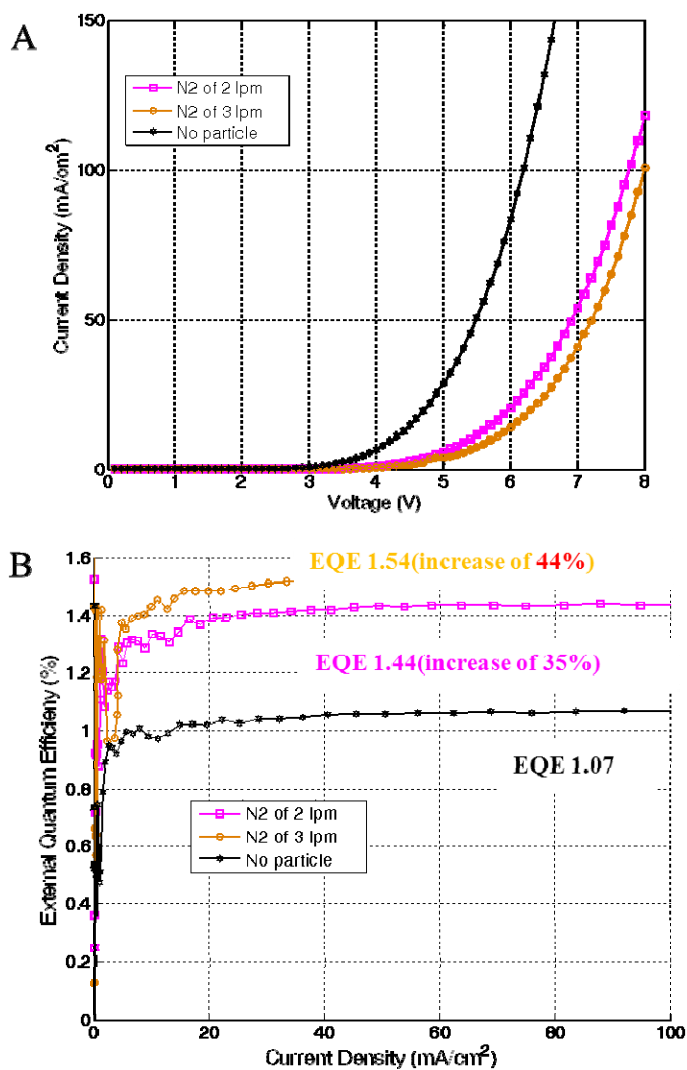


Figure 4.11. Characteristics of the OLED devices with respect to N_2 flow rate. (A) Characteristics of current density versus voltage driving the devices. (B) External quantum efficiency of the devices.

EQE could be affected by balance of charge carriers such as holes and electrons (γ), production efficiency of singlet for fluorophores (η_s), quantum efficiency of fluorescence (ϕ) and out-coupling efficiency (η_{oc}) which could be expressed in [Equation 4.6].

$$\eta_{ext} = \gamma \cdot \eta_s \cdot \phi \cdot \eta_{oc} \quad \text{[Equation 4.6]}$$

Production efficiency of singlet for fluorophores and quantum efficiency of fluorescence have been known to be difficult to control (Weixin Li et al. 2006). However, gold nanoparticles can affect quantum efficiency of fluorescence by localized surface plasmon resonance or quenching of the nanoparticles depending on the distance between the particles and fluorophores. Enhancement of EQE is thought to be based on LSPR phenomenon of nano-sized metal nanoparticles because absorption peak of nano-sized gold nanoparticles is known to be similar to emission peak of Alq3 in the OLED (Fujiki et al. 2010). In addition, the particles also can influence the balance of charge carriers by the degree of trapping or blocking holes in the hole-transfer layer. To explain the reason why use of nanoparticles enhances the EQE of OLED, photoluminescence (PL) of OLED with Au NPs was measured. The effect of the gold nanoparticles without enhancement of balance of charge carrier was evaluated. The structure for PL measurement was prepared to have ITO/NPB/Alq3 layer and the thickness of Alq3 was set 10 nm to prevent excessive quenching occurred when the layer was thinner than 10 nm, as shown in Fig. 4.12.

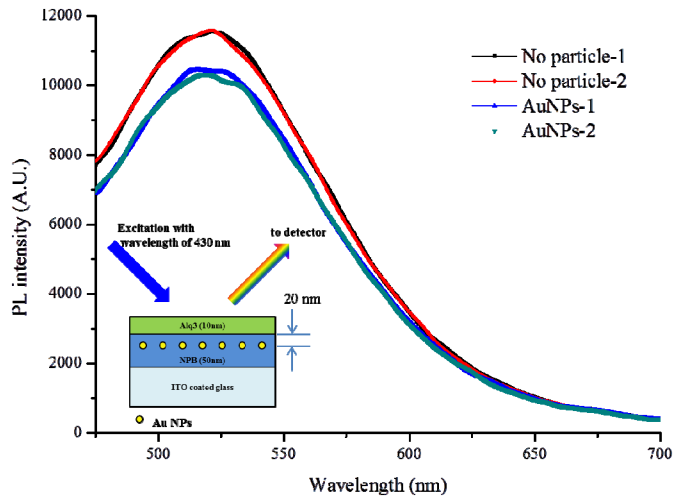


Figure 4.12. Photoluminescence spectra of the OLEDs with the particles deposited at the distance of 20 nm from the emitting layer and the OLED without the particles. Inset shows the schematic of photoluminescence measurement using excitation source wavelength of 430 nm.

Alq3 was excited by the wave source of 430nm to obtain PL spectra while NPB was not excited at the excitation wavelength. PL intensity for the OLED with the gold nanoparticles at the optimum position was reduced by about 13% at the wavelength of about 530 nm in comparison of the case of OLED without gold nanoparticles in Fig. 4.12. This shows that embedding gold nanoparticles into the OLED unexpectedly has a negative effect for enhancing the EQE of the OLED. Enhancement of EQE of OLED infers the existence of other effects. We paid attention to the balance of charge carriers and change in out-coupling efficiency. Extinction by gold nanoparticles was

measured using UV-Visible spectroscopy. Photons were absorbed into gold nanoparticle or scattered by the particles. For smaller particles smaller than 10nm, absorption is more dominant than scattering. (Kelly et al. 2003) Absorption in NPB layer with various sized nanoparticles was calculated using commercial FDTD (finite-difference time-domain) simulation, LumericalTM. In Fig. 4.13, absorption in NPB increased as sizes of the particles, which means that photons emitted from the emitting layer of OLED could become extinct by gold nanoparticles. Bigger particles or aggregates could absorb larger amount of photons emitted from the recombination of holes and electrons. Absorption of bigger nanoparticles could decrease luminescence of OLED and the resultant efficiency could diminish. For another factor to affect the EQE, gold nanoparticles could change the electric field in the organic layer in an OLED. Gold nanoparticles embedded in the NPB layer could be charged positively with amount of holes in the NPB layer due to charge trapping characteristic of metal nanoparticles. (Li et al, 2008) Corresponding electric fields in the OLED with charged gold nanoparticles were calculated with assumption that the nanoparticles were fully charged under the external fields, as shown in Fig. 4.14A and B. Electric fields shown in Fig. 4.14C infer the probability that positively charged gold nanoparticles could decrease the electric field at anode electrode so they block the hole injected from the ITO electrode of the OLED and enhance the electron injection from Al electrode. In some studies, insertion of oxide materials between the hole-transfer layer and ITO electrode blocked hole injection into the hole transfer layer and the

corresponding efficiency was improved. (Lu and Yokoyama 2003) In this experiment, gold nanoparticles in the NPB layer could carry out the same function as the case of oxide materials. This phenomenon could explain the enhancement of balance of holes and electrons injected into the OLED but could not elucidate the enhancement of EQE with respect to sizes of the nanoparticles. Noticeable difference with respect to sizes of the particles is the change in the area for recombination site of hole and electrons. Positively and fully charged gold nanoparticles repel the hole and confine the trajectories of the hole. As a result, the area for recombination of charge carriers decreased as sizes of the particles increased, as shown in Fig. 4.14. Therefore, Enhancement of luminescence efficiency could be attributed to optimization for the balance of charge carriers and the area reduction of recombination site rather than LSPR of gold nanoparticles. In addition, Higher EQE enhancement via less agglomerated and smaller particles in the experiment could be affected by quenching effects of metal nanoparticles. (Lakowicz 2001) Smaller sized particles could reduce the possibility of quenching by the particles with comparison to the case of bigger sized particles. The bigger sizes of the particles can cause fluorophores to close the surface of the particles at the same position and the resultant quenching effect become more dominant compared to smaller sized particles. Higher EQE of OLED could be accomplished by adding the smaller and less agglomerated gold nanoparticles even though luminescence enhancement did not be shown in PL experiment. These results mean that EQE could be affected by several factors such as balance of charge carriers, change in the

area of recombination site, dominant absorption of metal nanoparticle smaller than 10nm and quenching effect, which should be independently studied in order to expect the efficiency exactly. Quantitative analysis for these factors affecting the change in EQE is needed to study further when the particles are embedded into an OLED.

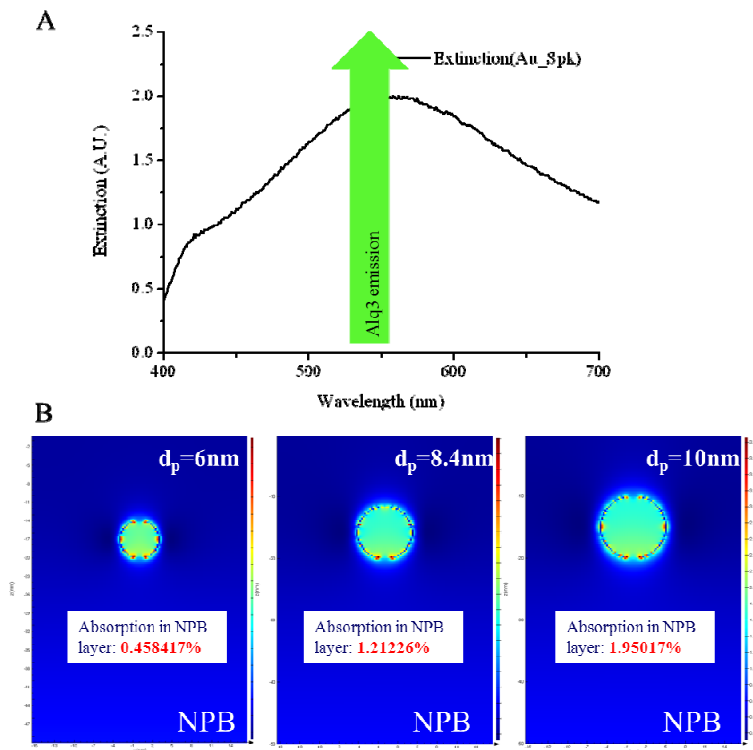


Figure 4.13. Extinction and absorption in the NPB layer with gold nanoparticles. (A) Extinction spectrum of gold nanoparticles deposited at the distance of 20 nm from the emitting layer in middle of the NPB layer. (B) Calculated absorption of NPB layer with gold nanoparticles with respect to size of a gold particle.

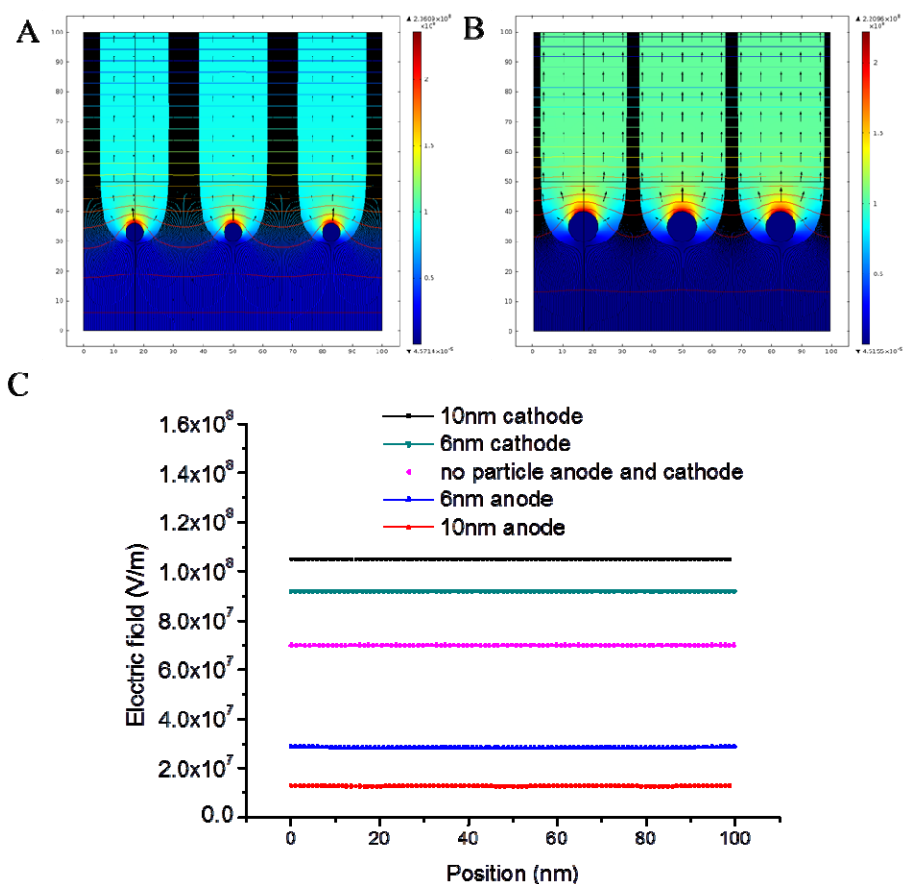


Figure 4.14. Electric fields in the OLED with fully charged gold nanoparticles and external potential of 7 V. (A) Electric fields in the OLED with 6 nm-sized gold nanoparticles at the distance of 20 nm from the emitting layer in middle of the NPB layer. (B) Electric fields in the OLED with 10 nm-sized gold nanoparticles at the same position as the case of 6 nm-sized particles. (C) Electric fields at cathode and anode with respect to particle sizes comparing to the case without the particles.

4.4. Conclusion

We fabricated organic light emitting diode with gold nanoparticles generated via pin-to-plate type spark discharge and demonstrated the change of external quantum efficiency (EQE) for OLED controlling sizes of the nanoparticles at the optimum position in the middle of organic materials of the OLED. In addition, effects of the particle size on EQE were considered in terms of several factors. In this experiment, EQE of the OLED with smallest gold nanoparticles at distance of 20 nm from the emitting layer increased up to a maximum of 44 % in comparison with OLED without gold nanoparticles. Enhancement of EQE can be attributed to optimization for the balance of charge carriers and the area reduction of recombination site even though luminescence enhancement did not be shown. Also, dominant absorption of gold nanoparticles smaller than 10 nm and quenching of metal nanoparticles near fluorophores could also affect the quantum efficiency of the OLED. Detailed analysis for several factors influencing luminescence efficiency is needed to study further.

4.5. References

- Campion, A., Kambhampati, P. (1998). Surface-enhanced Raman scattering. *Chemical Society Review*, 27, 241.
- Deng, Z., Ding, X., Lee, S. and Gambling, W. (1999). Enhanced brightness and efficiency in organic electroluminescent devices using SiO buffer layers. *Applied Physics Letters*, 74, 2227.
- Forrest, S. R., Bradley, D. D. C. and Thompson, M. E. (2003). Measuring the Efficiency of Organic Light Emitting Devices. *Advanced Materials*, 15, 1043-1048.
- Fort, E. and Grésillon, S. (2008). Surface enhanced fluorescence. *Journal of Physics D: Applied Physics*, 41, 013001.
- Fujiki, A., Uemura, T., Zettsu, N., Akai-Kasaya, M., Saito, A. and Kuwahara, Y. (2010). Enhanced fluorescence by surface plasmon coupling of Au nanoparticles in an organic electroluminescence diode. *Applied Physics Letters*, 96, 043307-043307-043303.
- Geddes, C. D. and Lakowicz, J. R. (2002). Editorial: Metal-enhanced fluorescence. *Journal of Fluorescence*, 12, 121-129.
- Henzie, J., Lee, J., Lee, M. H., Hasan, W. and Odom, T. W. (2009). Nanofabrication of Plasmonic Structures*. *Annual Review of Physical Chemistry*, 60, 147-165.
- Huang, F. M., Festy, F. and Richards, D. (2005). Tip-enhanced fluorescence imaging of quantum dots. *Applied Physics Letters*, 87, 183101.
- Hung, L. and Chen, C. (2002). Recent progress of molecular organic

- electroluminescent materials and devices. *Materials Science and Engineering: R: Reports*, 39, 143-222.
- Hutter, E., Fendler, J. H. (2004). Exploitation of Localized Surface Plasmon Resonance. *Advanced materials*, 16, 1685.
- Kelly, K. L., Coronado E., Zhao, L. L. and Schatz, G. C. (2003). The Optical Properties of Metal Nanoparticles: □ The Influence of Size, Shape, and Dielectric Environment. *Journal of physical chemistry B*, 107, 668-677
- Lakowicz, J. R. (2001). Radiative decay engineering: biophysical and biomedical applications. *Analytical Biochemistry*, 298, 1-24.
- Lichtman, J. W. and Conchello, J. A. (2005). Fluorescence microscopy. *Nature Methods*, 2, 910-919.
- Okamoto, K., Niki, I., Shvartser, A., Narukawa, Y., Mukai, T. and Scherer, A. (2004). Surface-plasmon-enhanced light emitters based on InGaN quantum wells. *Nature materials*, 3, 601-605.
- Ostrowski, J. C., Mikhailovsky, A., Bussian, D. A., Summers, M. A., Buratto, S. K. and Bazan, G. C. (2006). Enhancement of Phosphorescence by Surface □ Plasmon Resonances in Colloidal Metal Nanoparticles: The Role of Aggregates. *Advanced Functional Materials*, 16, 1221-1227.
- Schuller, J. A., Barnard, E. S., Cai, W., Jun, Y. C., White, J. S. and Brongersma, M. L. (2010). Plasmonics for extreme light concentration and manipulation. *Nature materials*, 9, 193-204.
- Sheats, J. R., Antoniadis, H., Hueschen, M., Leonard, W., Miller, J., Moon, R., Roitman, D. and Stocking, A. (1996). Organic electroluminescent devices. *Science*, 273, 884-888.

- Sung, H., Lee, J., Han, K., Kim, C. and Choi, M. (2012). , Quantun efficiency enhacement in a gold nanoparticle-embedded organic light emitting device engineering the particle position. In preparation.
- Tanaka, T., Totoki, Y., Fujiki, A., Zettsu, N., Miyake, Y., Akai-Kasaya, M., Saito, A., Ogawa, T. and Kuwahara, Y. (2011). Enhanced Red-Light Emission by Local Plasmon Coupling of Au Nanorods in an Organic Light-Emitting Diode. *Applied Physics Express*, 4, 2105.
- Tang, C. and VanSlyke, S. (1987). Organic electroluminescent diodes. *Applied Physics Letters*, 51, 913-915.
- Tang, C., VanSlyke, S. and Chen, C. (1989). Electroluminescence of doped organic thin films. *Journal of Applied Physics*, 65, 3610-3616.
- Xiao, Y., Yang, J. P., Cheng, P. P., Zhu, J. J., Xu, Z. Q., Deng, Y. H., Lee, S. T., Li, Y. Q. and Tang, J. X. (2012). Surface plasmon-enhanced electroluminescence in organic light-emitting diodes incorporating Au nanoparticles. *Applied Physics Letters*, 100, 013308.
- Yang, K. Y., Choi, K. C. and Ahn, C. W. (2009). Surface plasmon-enhanced energy transfer in an organic light-emitting device structure. *Optics Express*, 17, 11495-11504.
- Zhi-Feng, Z., Zhen-Bo, D., Chun-Jun, L., Meng-Xin, Z. and Deng-Hui, X. (2003). Organic light-emitting diodes with a nanostructured TiO₂ layer at the interface between ITO and NPB layers. *Displays*, 24, 231-234.

This page is intended to be blank

Chapter 5.

Concluding Remarks

In this study, we developed an unconventional type spark discharge generator to produce unagglomerated charged metal aerosols for the IAAL and overcame the limitation of the IAAL for charged particle patterning even on a non-conducting substrate. Furthermore, the aerosols via the generator were exploited to fabricate nanoparticle embedded OLED for enhancement of emission efficiency.

In Ch. 2, we demonstrated that the pin-to-plate type spark discharge generator could produce much smaller unagglomerated charged metal aerosols with a narrower size distribution at higher concentration in comparison to the conventional rod-to-rod type generators. We examined and compared the size and charge distributions of particles for In-Sn alloy, silver and copper, and investigated spark parameters and flow patterns for each configuration to explain the observed results. Much faster transport of as-generated particles in the use of pin-to-plate type electrode configuration could explain why smaller and unagglomerated charged aerosols are produced via our spark discharge generator in comparison to the rod-to-rod type generator. It was also found that charge distribution of generated particles via the rod-to-rod type generator was changed with respect to spark frequency because electro-deposition of charged particles onto the positive electrode became dominant during spark discharge. In contrast, similar charge distribution of particles for each polarity was obtained via pin-to-plate type spark discharge generator. It seems that losses of charged particles onto electrodes could change with the potential of electrode during spark

relaxation time with respect to spark frequency. Characteristics of the charge distribution with respect to spark frequency could be also affected by transport of particles by carrier gas.

The method for focused patterning of charged particles on a non-conducting substrate was proposed in Ch. 3. The temporary path to neutralize the charge of particles was devised to eliminate the charges from incoming charged particles by forming the conductive liquid film on the substrate. Surfactant to change the hydrophobic surface into hydrophilic one was used, which played a critical role of forming the liquid film. Droplets of conducting liquid via electrospray formed the thin film on the hydrophilic surface of the substrate. Nano and micro scale focused patterns was demonstrated with PSL particles via this method, and conducting micro wires with silver nanoinks were obtained with a higher resolution in compared to normal inkjet technology. Sub-micro scale gold nanoparticle patterns were also realized with charged particles via spark discharge generator.

Lastly, unagglomerated gold aerosols via the pin-to-plate type spark discharge generator were utilized to fabricate nanoparticle embedded OLED for increasing the external quantum efficiency. The gold aerosols can be easily embedded in the middle of organic materials of OLED by controlling deposition position of the particles from the emitting layer of OLED without damage to the organic material. Optimum distance and size of the particles were found to maximize EQE of OLED with the corresponding EQE enhancement of about 44 %. Enhancement of luminescence efficiency could

be attributed to the optimization for the balance of charge carriers and the area reduction of recombination site rather than LSPR of gold nanoparticles. In addition, absorption and quenching effect by gold nanoparticles smaller than 10 nm could also affect the quantum efficiency.

Acknowledgement

This work was funded by the Global Frontier Center for Multiscale Energy System supported by the Ministry of Education, Science and Technology, Korea. Supports from BK21 program and WCU (World Class University) multiscale mechanical design program (R31-2008-000-10083-0) through the Korea Research Foundation funded by the Ministry of Education, Science and Technology are also gratefully acknowledged. I would like to thank W. Kim, K. Jung, H. Sung, J. Lee, Prof. C. Kim and Dr. Peter V. Pikhitsa for their helps and ideas for this study.

Abstract (in Korean)

스파크방전을 이용한 하전 에어로졸 발생 및 그 응용

서울대학교 대학원 기계항공공학부
한 규 희

요약

나노입자는 그 고유한 특성으로 나노공학분야에서 널리 연구되고 있다. 신뢰성있는 나노입자 패터닝 기술은 나노입자의 실질적 이용에 있어 선행조건이 되며 이는 기존 포토리소그래피기술의 대안으로 될 수 있다. 이온기반 에어로졸 리소그래피를 이용한 고정밀, 병렬식의 하전입자 패터닝기술은 전도성 기판에 2차원 패터닝뿐만 아니라 독창적인 3차원 나노입자구조의 패터닝이 가능하다. 이러한 이온기반 에어로졸 패터닝을 위한 안정적인 하전입자의 발생과 기판 종류에 관계없이 하전입자를 패터닝하는 기술은 본 에어로졸 패터닝 기술의 활용을 더욱 확대할 수 있다. 이 연구의 목적은 이온기반 패터닝을 위해 일반적인 구조와 다른 독창적인 스파크방전 장치로 하전입자를 발생시키고 기존 이온기반 패터닝 기술의 비전도성 기판에 대한 한계를 극복하는데 있다. 신규 개발한 스파크 방전장치로 만든 하전입자를 유기 발광 다이오드 내부에 내장시켜 발광효율을 증가시키기 위해 이용하였다.

일반적인 대칭 전극 구조를 갖는 스파크 방전장치와 달리 핀(pin)과 판(plate)형상의 전극구조를 갖는 스파크 방전장치로 더 크기가 작고 응집이 적은 하전 에어로졸을 크기 산포도 더 작게 발생시킬 수 있다. 인듐-주석합금, 은, 구리에 대한 크기와 하전 분포를 스파크 방전장치 구조에 따라 측정하고 비교하였다. 측정된 하전입자의 발생특성을 설명하기 위해 방전장치 구조별 스파크 방전 인자와 유동 특성에 대해 연구하였다. 핀-판 구조의 스파크 방전장치 내에서 발생한 입자의 빠른 배출특성이 더 작고 응집이 적은 나노입자를 발생하는데 중요한 역할을 한다. 또한 새로 개발한 스파크 방전장치와 달리 일반적인 스파크 방전장치는 스파크 발생주파수에 따라 하전입자가 스파크 전극으로의 전착이 달라지기 때문에 하전입자의 분포 상태가 변함을 알 수 있었다.

나노입자 집속마스크를 이용하여 비전도성 기판위에 하전입자를 패터닝하는 기술을 개발하였다. 계면활성제와 정전분무로 공급되는 전도성 액적을 이용하여 비전성기판상에 임시적인 전도성 액체막을 형성하고 기판위에 부착되는 하전입자를 전기적으로 중화시켜 하전입자 패터닝을 구현하였다. PSL 나노입자를 이용하여 유연기판과 유리기판에 나노와 마이크로 스케일의 패턴을 구현했으며 은 나노잉크로 기존 잉크젯 기술 보다 고정밀의 전도성 와이어도 구현하였다. 본 기술로 스파크 방전장치로 발생시킨 금속 하전입자를 가지고 나노 스케일의 패터닝까지 최종적으로 구현하였다.

핀-판 전극 구조를 갖는 스파크 방전 장치로 발생한 응집이 적은 금 나노입자를 유기발광 다이오드에 적용하여 외부 양자 효율을

증가시키는데 응용하였다. 발광 다이오드 내에 유기물의 손상없이 금 입자를 위치시키는 것이 가능하며 이미 알려진 최적의 위치에서 최적의 크기를 찾아 외부 양자 효율을 44%까지 향상시켰다. 이러한 발광 다이오드의 효율 향상은 금 나노입자가 내장된 유기발광 다이오드 안으로 주입되는 정공과 전자 개수의 균형과 전자와 정공이 재결합하는 장소의 면적 변화에 대한 최적화에 기인한 것으로 판단된다.

주요어: 스파크 방전, 하전 에어로졸, 이온기반 에어로졸 리소그래피, 유기 발광 다이오드

학 번: 2008-30202